

PREPARED FOR SUBMISSION TO JCAP

Affleck-Dine leptogenesis scenario for resonant production of sterile neutrino dark matter

Kentaro Kasai,^a Masahiro Kawasaki,^{a,b} and Kai Murai^c

^aICRR, University of Tokyo, Kashiwa, 277-8582, Japan

^bKavli IPMU (WPI), UTIAS, University of Tokyo, Kashiwa, 277-8583, Japan

^cDepartment of Physics, Tohoku University, Sendai, 980-8578, Japan

E-mail: kkasai@icrr.u-tokyo.ac.jp, kawasaki@icrr.u-tokyo.ac.jp,
kai.murai.e2@tohoku.ac.jp

Abstract. Sterile neutrino is a fascinating candidate for dark matter. In this paper, we examine the Affleck-Dine (AD) leptogenesis scenario generating a large lepton asymmetry, which can induce the resonant production of sterile neutrino dark matter via the Shi-Fuller (SF) mechanism. We also revisit the numerical calculation of the SF mechanism and the constraints from current X-ray and Lyman- α forest observations. We find that the AD leptogenesis scenario can explain the production of sterile neutrino dark matter by incorporating a non-topological soliton with a lepton charge called L-ball. Finally, we discuss an enhancement of second-order gravitational waves at the L-ball decay and investigate the testability of our scenario with future gravitational wave observations.

Keywords: physics of the early universe, dark matter, supersymmetry and cosmology

Contents

1	Introduction	1
2	Numerical study of Shi-Fuller mechanism revisited	2
2.1	Shi-Fuller mechanism	2
2.2	Numerical setup	5
2.3	Analytical study	7
2.4	Numerical results	8
2.5	Validity of the stationary point approximation	10
3	Large lepton asymmetry from Affleck-Dine mechanism	12
3.1	Affleck-Dine leptogenesis	12
3.2	Delayed-type L-ball scenario	14
4	Observational implications	17
4.1	Free-streaming length of sterile neutrinos	17
4.2	Gravitational wave enhancement at L-ball decay	20
5	Conclusion	23
A	Fitting function for y_e	23
B	Numerical dependence on the number of bins used in momentum space	24
C	Analytical estimate of the sterile neutrino spectrum	25
D	Review of gravitational waves enhanced at the L-ball decay	27

1 Introduction

Sterile neutrinos with masses of the keV scale are one of the attractive candidates for dark matter (for a review, see Refs. [1, 2]). Sterile neutrinos can be produced via mixing with the standard model (SM) neutrinos (“active” neutrinos) [3–6]. The simplest and most well-known mechanism to produce sterile neutrino dark matter is the Dodelson-Widrow (DW) mechanism [3, 7]. In this mechanism, sterile neutrinos are produced through neutrino oscillations between active and sterile neutrinos in the early universe. However, this scenario is excluded by X-ray observations of the radiative decay of sterile neutrinos [5, 8–12] and by Lyman- α constraints from structure formation [13, 14].

An alternative scenario is the resonant production of sterile neutrinos called the Shi-Fuller (SF) mechanism [6]. This mechanism assumes a non-zero lepton asymmetry in the active neutrino sector. Then, the effective mixing angle between active and sterile states is resonantly enhanced at a certain cosmic temperature due to the lepton asymmetry. Consequently, we can explain all dark matter with a smaller vacuum mixing angle between active and sterile states than that required in the DW mechanism [4, 5, 15–19]. Thus, we expect that

this scenario evades the constraints from X-ray observations. Importantly, this scenario requires a lepton-to-entropy ratio $\gtrsim \mathcal{O}(10^{-5})$ much larger than the observed baryon-to-entropy ratio ($\sim 10^{-10}$) to account for all dark matter through the resonance effect.

The possibility of such a large lepton asymmetry is also well motivated by the recent observation of helium-4 in metal-poor galaxies, which suggests the existence of a large lepton asymmetry before big bang nucleosynthesis (BBN) [20]. However, if the lepton asymmetry is generated when the sphaleron process is in chemical equilibrium, baryon and lepton asymmetries must be of the same order. Therefore, we must consider the scenario in which the large lepton asymmetry is generated after the electroweak phase transition.

In this paper, we consider the Affleck-Dine (AD) leptogenesis scenario for the production of a large lepton asymmetry. In this scenario, the lepton charge is confined in non-topological solitons called L-balls and is protected against the sphaleron process. Afterward, L-balls decay and release the lepton charge to the thermal plasma after the electroweak phase transition [21, 22]. This scenario can account for a lepton-to-entropy ratio as large as $\mathcal{O}(10^{-3})$ in contrast to leptogenesis through the decay of heavy sterile neutrinos, which typically explains a lepton-to-entropy ratio of at most $\sim 7 \times 10^{-4}$ [23].

Interestingly, our scenario has another observational implication. To produce a large lepton asymmetry the L-balls dominate the energy density in the universe before the decay. Since a sudden transition from a matter-dominated era to a radiation-dominated era occurs at L-ball decay, gravitational waves generated from the second-order effect of the scalar mode are enhanced on small scales. We investigate the testability of our scenario by future observations of gravitational waves through μ Ares [24], and THEIA [25].

In this paper, we also revisit the numerical calculation of the SF mechanism to discuss the observational constraint. We numerically evaluate the required vacuum mixing angle between the active and sterile states for a given sterile neutrino mass m_s and the initial lepton asymmetry in the active neutrino sector to explain all dark matter. In this calculation, we take into account the time dependence of the relativistic degree of freedom, which is intrinsically important because the resonance occurs around the QCD phase transition for the parameters of interest. We find that the lepton-to-entropy ratio is required to be $\gtrsim \mathcal{O}(10^{-4})$ to evade both the X-ray and Lyman- α constraints.

The rest of this paper is organized as follows. In Sec. 2, we review the production of sterile neutrinos through the SF mechanism and show the numerical results. We explain the leptogenesis in the AD mechanism in Sec. 3. We discuss the observational implications of our scenario in Sec. 4. Sec. 5 is devoted to the conclusion of our results.

2 Numerical study of Shi-Fuller mechanism revisited

In this section, we revisit the numerical calculation of sterile neutrino production by the SF mechanism, which was originally proposed in Ref. [6] (see also Refs. [4, 15–19, 26]).

2.1 Shi-Fuller mechanism

First, we derive the basic equations of the SF mechanism following the discussion in Ref. [27]. Here, we consider the mixing between one generation of sterile neutrinos and one flavor of active neutrinos for simplicity. Then, the sterile neutrino state mixes with the active neutrino state as

$$\begin{aligned} |\nu_a\rangle &= \cos\theta |\nu_1\rangle + \sin\theta |\nu_2\rangle \ , \\ |\nu_s\rangle &= -\sin\theta |\nu_1\rangle + \cos\theta |\nu_2\rangle \ , \end{aligned} \tag{2.1}$$

where $|\nu_a\rangle$ and $|\nu_s\rangle$ denote the active and sterile neutrino states, respectively, and $|\nu_1\rangle$ and $|\nu_2\rangle$ denote the two mass eigenstates.

The effective description of the kinetic equation of neutrino states is given as [23, 27]

$$i(\partial_t - Hp\partial_p)\rho = [\mathcal{H}, \rho] - i\{\Gamma, \rho - \rho_{\text{eq}}\}, \quad (2.2)$$

where H is the Hubble parameter, p is the physical momentum, \mathcal{H} is the Hamiltonian, and $[\cdot, \cdot]$ and $\{\cdot, \cdot\}$ denote commutation and anti-commutation relations, respectively. Here, ρ is the density operator in the flavor basis, i.e., the active and sterile neutrinos, and its components are written as

$$\rho(t, p) = \begin{pmatrix} \rho_{aa} & \rho_{as} \\ \rho_{as}^* & \rho_{ss} \end{pmatrix}. \quad (2.3)$$

Here, ρ_{aa} and ρ_{ss} correspond to the distribution function of the active and sterile neutrinos, respectively, and ρ_{as}^* is the complex conjugate of ρ_{as} . ρ_{eq} is the thermal distribution given by

$$\rho_{\text{eq}} = \begin{pmatrix} f_{\text{eq}}(\sqrt{m_a^2 + p^2}, \mu_{\nu_a}) & 0 \\ 0 & f_{\text{eq}}(\sqrt{m_s^2 + p^2}, \mu_{\nu_s}) \end{pmatrix}, \quad (2.4)$$

where m_a and m_s are the active and sterile neutrino masses, respectively, $f_{\text{eq}}(E, \mu) \equiv 1/(\exp[(E - \mu)/T] + 1)$ is the Fermi-Dirac distribution function, and μ_{ν_a} and μ_{ν_s} are the chemical potentials of the active and sterile neutrinos, respectively. In the following, we approximate that $\sqrt{m_a^2 + p^2} \simeq \sqrt{m_s^2 + p^2} \simeq p$ since both the active and sterile neutrinos are relativistic at the epoch of interest. Γ is a Hermitian matrix associated with the scattering rate of neutrinos in the thermal plasma. Since sterile neutrinos do not interact with the thermal plasma, Γ has a form written as

$$\Gamma = \frac{1}{2} \begin{pmatrix} \Gamma_{\nu_a} & 0 \\ 0 & 0 \end{pmatrix}, \quad (2.5)$$

where Γ_{ν_a} is the total thermal width of the active neutrino given by

$$\Gamma_{\nu_a}(p, T) = y_a(T)G_{\text{F}}^2 p T^4. \quad (2.6)$$

Here, G_{F} is the Fermi coupling constant, and $y_a(T)$ is a factor depending on the degrees of freedom in the thermal plasma. In the flavor basis, the Hamiltonian \mathcal{H} is written as

$$\mathcal{H} = \begin{pmatrix} V_a - \frac{m_s^2}{4p} \cos 2\theta & \frac{m_s^2}{4p} \sin 2\theta \\ \frac{m_s^2}{4p} \sin 2\theta & \frac{m_s^2}{4p} \cos 2\theta \end{pmatrix}, \quad (2.7)$$

where V_a denotes the effective potential due to the finite temperature and density effects on the self-energy of the active neutrino. The first term in the right-hand side of Eq. (2.2) describes the neutrino oscillation effect, and the second term describes the scattering process of active neutrinos.

Consequently, Eq. (2.2) can be rewritten as

$$i(\partial_t - Hp\partial_p)\rho_{aa} = \frac{m_s^2}{4p} \sin 2\theta (\rho_{as}^* - \rho_{as}) - i\Gamma_{\nu_a}(\rho_{aa} - f_{\text{eq}}), \quad (2.8)$$

$$i(\partial_t - Hp\partial_p)\rho_{ss} = \frac{m_s^2}{4p} \sin 2\theta (\rho_{as} - \rho_{as}^*), \quad (2.9)$$

$$i(\partial_t - Hp\partial_p)\rho_{as} = \frac{m_s^2}{4p} \sin 2\theta (\rho_{ss} - \rho_{aa}) + \left(V_a - \frac{m_s^2}{2p} \cos 2\theta - i\frac{\Gamma_{\nu_a}}{2} \right) \rho_{as}. \quad (2.10)$$

Since Γ_{ν_a} is much larger than H and m_s^2/p for the temperatures of interest, Eq. (2.8) leads to $\rho_{aa} \simeq f_{\text{eq}}(p, \mu_{\nu_a})$. Furthermore, we assume that the left-hand side of Eq. (2.10) vanishes. This is called stationary point approximation [27], and we will discuss the validity of this approximation in Sec. 2.5. Under the stationary point approximation, we obtain

$$(\partial_t - Hp\partial_p)\rho_{ss} = \frac{1}{4}\Gamma_{\nu_a} \sin^2 2\theta \left[\left(\cos 2\theta - \frac{2p}{m_s^2} V_a \right)^2 + \frac{p^2}{m_s^4} \Gamma_{\nu_a}^2 \right]^{-1} (\rho_{aa} - \rho_{ss}). \quad (2.11)$$

Similarly, the distribution function of the anti-sterile neutrino follows

$$(\partial_t - Hp\partial_p)\rho_{\bar{s}\bar{s}} = \frac{1}{4}\Gamma_{\nu_a} \sin^2 2\theta \left[\left(\cos 2\theta - \frac{2p}{m_s^2} V_{\bar{a}} \right)^2 + \frac{p^2}{m_s^4} \Gamma_{\nu_a}^2 \right]^{-1} (\rho_{\bar{a}\bar{a}} - \rho_{\bar{s}\bar{s}}), \quad (2.12)$$

where $V_{\bar{a}}$ is the effective potential of the anti-active neutrino. Here, we approximated the scattering rate of the anti-active neutrino by Γ_{ν_a} since the contribution from the chemical potential μ_{ν_a} is negligible.

To solve the Boltzmann equation, it is convenient to define a comoving momentum $\propto pa$. From the conservation of the total entropy density, we define a dimensionless comoving momentum by

$$\epsilon \equiv \left(\frac{g_{*,s}(T_i)}{g_{*,s}(T)} \right)^{1/3} \frac{p}{T}, \quad (2.13)$$

where $g_{*,s}$ is the effective number of relativistic degrees of freedom for entropy, T is cosmic temperature, and T_i is the reference temperature. Note that ϵ is generally different from $\epsilon_{\text{phys}} \equiv p/T$ due to the time evolution of $g_{*,s}$.

Defining $f_{\nu_a} \equiv \rho_{aa}$, $f_{\bar{\nu}_a} \equiv \rho_{\bar{a}\bar{a}}$, and $f_{\nu_s} \equiv \rho_{ss} + \rho_{\bar{s}\bar{s}}$, and using Eqs. (2.11) and (2.12), we obtain the production rate of sterile neutrinos as

$$\frac{d}{dt} f_{\nu_s}(\epsilon, T) = \Gamma_{\nu_a}(p, T) [\theta_M^2(\epsilon, T) f_{\nu_a}(\epsilon, T) + \bar{\theta}_M^2(\epsilon, T) f_{\bar{\nu}_a}(\epsilon, T)], \quad (2.14)$$

where θ_M and $\bar{\theta}_M$ are effective mixing angle in the thermal plasma defined by

$$\begin{aligned} \theta_M^2(\epsilon, T) &\equiv \theta^2 \left[\left(1 - \frac{2p}{m_s^2} V_a(\epsilon, T) \right)^2 + \frac{p^2 \Gamma_{\nu_a}^2(\epsilon, T)}{m_s^4} \right]^{-1}, \\ \bar{\theta}_M^2(\epsilon, T) &\equiv \theta^2 \left[\left(1 - \frac{2p}{m_s^2} V_{\bar{a}}(\epsilon, T) \right)^2 + \frac{p^2 \Gamma_{\nu_a}^2(\epsilon, T)}{m_s^4} \right]^{-1}. \end{aligned} \quad (2.15)$$

Here, we used the approximations of $\cos \theta \simeq 1$ and $\sin \theta \simeq \theta$, and used $f_{\nu_a}, f_{\bar{\nu}_a} \gg f_{\nu_s}$, which holds for the parameter region of our interest. The thermal self-energies of the active and anti-active neutrinos, V_a and $V_{\bar{a}}$, are respectively given by [28]

$$\begin{aligned} V_a &= \sqrt{2}G_{\text{F}} \left(2(n_{\nu_a} - n_{\bar{\nu}_a}) + \sum_{b \neq a} (n_{\nu_b} - n_{\bar{\nu}_b}) \right) - B_a p T^4 \\ &= \sqrt{2}G_{\text{F}} \left(2L_{\nu_a} + \sum_{b \neq a} L_{\nu_b} \right) s_{\text{tot}} - B_a \epsilon_{\text{phys}}(T) T^5, \\ V_{\bar{a}} &= \sqrt{2}G_{\text{F}} \left(-2(n_{\nu_a} - n_{\bar{\nu}_a}) + \sum_{b \neq a} (-n_{\nu_b} + n_{\bar{\nu}_b}) \right) - B_a p T^4 \\ &= -\sqrt{2}G_{\text{F}} \left(2L_{\nu_a} + \sum_{b \neq a} L_{\nu_b} \right) s_{\text{tot}} - B_a \epsilon_{\text{phys}}(T) T^5, \end{aligned} \quad (2.16)$$

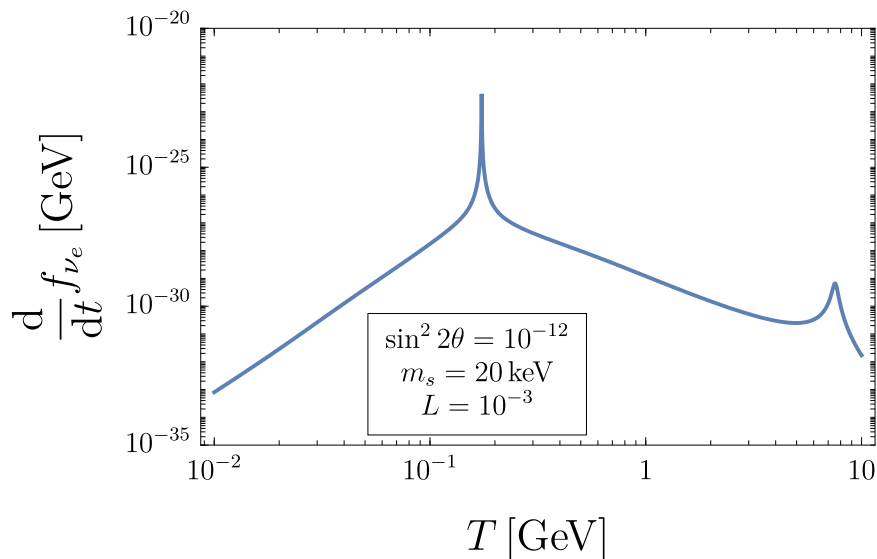


Figure 1. Production rate of sterile neutrinos df_{ν_s}/dt for $\epsilon = 1$ with $T_i = 1$ GeV, $\sin^2 2\theta = 10^{-12}$, $m_s = 20$ keV, and $L = 10^{-3}$. We see that there are two resonance points at $T \sim 0.2$ GeV and $T \sim 7$ GeV.

where n_{ν_a} and $n_{\bar{\nu}_a}$ are the number densities of ν_a and $\bar{\nu}_a$, respectively, and s_{tot} is the total entropy density. Here, the subscripts a, b ($= e, \mu, \tau$) denote the flavors of the active neutrinos, and B_a is a constant taking a value of $B_e = 10.88 \times 10^{-9}$ GeV $^{-4}$ for $a = e$ [29]. We defined a lepton asymmetry parameter $L_{\nu_a} \equiv (n_{\nu_a} - n_{\bar{\nu}_a})/s_{\text{tot}}$. We neglected the contributions of the baryon and charged lepton sectors because they are much smaller than that of the active neutrino sector as discussed in Refs. [18, 19].

If there is no lepton asymmetry, V_a and $V_{\bar{a}}$ are equal and negative ($V_a = V_{\bar{a}} < 0$), and hence ν_s and $\nu_{\bar{s}}$ are produced with the same amount via the DW mechanism. On the other hand, if $L \equiv 2L_{\nu_e} + \sum_{b \neq e} L_{\nu_b} > 0$ is large enough, V_a becomes positive and θ_M is enhanced at some temperature. Consequently, ν_s is resonantly produced while the production of $\nu_{\bar{s}}$ is not so different from the DW mechanism. If $L < 0$, $\nu_{\bar{s}}$ can be resonantly produced in a similar way. This is how sterile neutrinos are produced in the SF mechanism. We show df_{ν_s}/dt for $\epsilon = 1$ and a fixed value of L in Fig. 1. Here, we assumed that sterile neutrinos have a mixing only with electron neutrinos. We see that there are two resonance points. As we will discuss in Sec. 2.3, the resonance at the lower temperature is generally more important when the resonance effect is dominant in production. Note that the production rate df_{ν_s}/dt in the realistic situation is different from that shown in Fig. 1 because the lepton asymmetry evolves in time.

2.2 Numerical setup

In this section, we explain the physical assumptions and the setup in our calculation of the SF mechanism. In numerical calculations, we focus on the mixing between electron neutrinos and sterile neutrinos.

First of all, we assume that active neutrinos of all flavors $a = e, \mu, \tau$ are in thermal

equilibrium and have the Fermi-Dirac distribution given by

$$\begin{aligned} f_{\nu_a}(\epsilon, T) &= [1 + \exp(\epsilon_{\text{phys}}(T) - \xi_{\nu_a}(T))]^{-1} , \\ f_{\bar{\nu}_a}(\epsilon, T) &= [1 + \exp(\epsilon_{\text{phys}}(T) + \xi_{\nu_a}(T))]^{-1} , \end{aligned} \quad (2.17)$$

where $\xi_{\nu_a}(T) \equiv \mu_{\nu_a}/T$ is the dimensionless chemical potential of the active neutrinos and is related to the lepton asymmetry as

$$\xi_{\nu_a}(T) = \frac{4\pi^2}{15} g_{*,s}(T) L_{\nu_a}(T) . \quad (2.18)$$

As we will discuss in Sec. 3.1, we consider the situation where the initial lepton asymmetry is given by $L_{\nu_e}^{\text{init}} = L_{\nu_\mu}^{\text{init}} = -L_{\nu_\tau}^{\text{init}}$ or $L_{\nu_e}^{\text{init}} = -L_{\nu_\mu}^{\text{init}} = L_{\nu_\tau}^{\text{init}}$. When the cosmic temperature is below $\mathcal{O}(10)$ MeV, the lepton asymmetry in each flavor is forced to be equal through neutrino oscillations among active neutrinos [30, 31]. As we will see later, the resonant production of sterile neutrinos occurs at $T > \mathcal{O}(10)$ MeV in our setup. Therefore, in the following, we consider that only L_{ν_e} evolves in time due to sterile neutrino production while L_{ν_μ} and L_{ν_τ} remain constant.

The time evolution of L_{ν_e} is given by

$$\frac{d}{dt} L_{\nu_e}(T) = -\frac{45}{4\pi^4 g_{*,s}(T_i)} \int d\epsilon \epsilon^2 \Gamma_{\nu_e}(p, T) [\theta_M^2(\epsilon, T) f_{\nu_e}(\epsilon, T) - \bar{\theta}_M^2(\epsilon, T) f_{\bar{\nu}_e}(\epsilon, T)] . \quad (2.19)$$

We solve Eqs. (2.14) and (2.19) simultaneously. As for the time dependence of the thermal width Γ_{ν_e} , we use a fitting function for $y_e(T)$ obtained from the result of Refs. [32, 33]. The details of our fitting function are presented in Appendix A. In the numerical calculations, we discretize ϵ . Since the resonance occurs in a narrow range of ϵ , a large number of the ϵ bins is required to assure the accuracy of the numerical calculations. We describe the details of the discretization in Appendix B.

Since the resonant production of sterile neutrinos occurs in the radiation-dominated era, the relation between the cosmic time and the cosmic temperature is given by

$$\frac{dt}{dT} = -\sqrt{\frac{90}{\pi^2 g_*(T)}} \frac{M_{\text{Pl}}}{T^3} \left(1 + \frac{1}{3} \frac{d \ln g_{*,s}(T)}{d \ln T} \right) , \quad (2.20)$$

where $M_{\text{Pl}} \simeq 2.4 \times 10^{18}$ GeV is the reduced Planck mass, and g_* is the number of relativistic degrees of freedom for energy. Hereafter, we assume that $g_* = g_{*,s}$ for $T \gtrsim 1$ MeV. Because the resonant production occurs around the QCD phase transition in our setup, the time dependence of g_* can affect the sterile neutrino abundance. We used the fitting formula of g_* presented in Ref. [34].

The final density parameter of the sterile neutrino, Ω_{ν_s} , is given by

$$\Omega_{\nu_s} = \frac{m_s T_0^3}{2\pi^2 \rho_{\text{cr},0}} \frac{g_{*,s}(T_0)}{g_{*,s}(T_i)} \int d\epsilon \epsilon^2 f_{\nu_s}(\epsilon, T = T_*) , \quad (2.21)$$

where $T_0 = 2.73$ K is the current cosmic temperature, $\rho_{\text{cr},0}$ is the current critical energy density of the universe, and $T_* = 1$ MeV is the final temperature of the numerical calculation.

2.3 Analytical study

Before showing the results of the numerical calculation, we analytically discuss the properties of the equation (2.14) that determines the evolution of the sterile neutrino density. In the SF mechanism, sterile neutrinos are mainly produced around the resonance point determined by

$$1 - \frac{2\epsilon_{\text{phys}}(T)T}{m_s^2} V_e(\epsilon, T) = 0$$

$$\Leftrightarrow 1 - \frac{8\sqrt{2}\pi^2 g_*(T) G_F \epsilon_{\text{phys}}(T) L_{\nu_e} T^4}{45 m_s^2} + 2B_e \frac{\epsilon_{\text{phys}}^2(T) T^6}{m_s^2} = 0. \quad (2.22)$$

This equation has at most two positive solutions for T , which we denote by $T = T_{\text{low}}$ and T_{high} ($T_{\text{low}} < T_{\text{high}}$).

Since T_{low} is approximately given by equating the first and second terms in Eq. (2.22), we find

$$T_{\text{low}} \propto \frac{m_s^{1/2}}{L_{\nu_e}^{1/4} \epsilon^{1/4}}. \quad (2.23)$$

Thus, the resonance at the lower temperature occurs from low to high ϵ modes. On the other hand, T_{high} is given by equating the second and third terms in Eq. (2.22), and its parameter dependence is given by

$$T_{\text{high}} \propto \frac{L_{\nu_e}^{1/2}}{\epsilon^{1/2}}. \quad (2.24)$$

In the non-resonant production case (the DW case), the second term in Eq. (2.22) is absent, and the peak temperature of sterile neutrino production is approximately given by equating the first and third term in Eq. (2.22). Note that in general T_{low} is smaller than the peak temperature in the DW mechanism for the same value of m_s and ϵ . Thus, if the resonance effect plays a dominant role, the production of sterile neutrinos typically takes place at a lower cosmic temperature than in the DW case.

Neglecting the time evolution of the lepton asymmetry during the resonance of a single mode and the production from anti-electron neutrinos, the integration can be performed analytically, which gives

$$f_{\nu_s} \simeq 0.96 \frac{g_*(T_i)^{2/3}}{g_*(T_{\text{low}})^{13/6}} \frac{M_{\text{Pl}} m_s^4 \theta^2}{G_F \epsilon^2 T_{\text{low}}^7} \frac{f_{\nu_e}(\epsilon, T_{\text{low}})}{L_{\nu_e}(T_{\text{low}})}, \quad (2.25)$$

for the resonance at $T = T_{\text{low}}$. For the resonance at $T = T_{\text{high}}$, we obtain

$$f_{\nu_s} \simeq 1.9 \frac{g_*(T_i)^{2/3}}{g_*(T_{\text{high}})^{13/6}} \frac{M_{\text{Pl}} m_s^4 \theta^2}{G_F \epsilon^2 T_{\text{high}}^7} \frac{f_{\nu_e}(\epsilon, T_{\text{high}})}{L_{\nu_e}(T_{\text{high}})}. \quad (2.26)$$

See Appendix C for the derivations of these formulae.

Since Eq. (2.25) is larger than Eq. (2.26) by a factor of $\mathcal{O}((T_{\text{high}}/T_{\text{low}})^7)$, we can approximate f_{ν_s} by Eq. (2.25) if $T_{\text{high}}/T_{\text{low}}$ is sufficiently large. Then, from Eqs. (2.23) and (2.25), we find

$$f_{\nu_s} \propto \frac{m_s^{1/2} L_{\nu_e}^{3/4} \theta^2}{\epsilon^{1/4}} f_{\nu_e}. \quad (2.27)$$

This indicates that the final abundance of the sterile neutrino monotonically increases with $L_{\nu_e}^{\text{init}}$ as long as the resonance effect plays a dominant role. If the time evolution of L_{ν_e} is

negligible, the final distribution is proportional to $\epsilon^{-1/4} f_{\nu_e}$ at $T \sim T_{\text{low}}$, which makes the average momentum smaller than the thermal distribution. On the other hand, if the time evolution of L_{ν_e} is significant, the value of L_{ν_e} at the resonant production monotonically decreases for ϵ since the resonance occurs from low ϵ to high ϵ . Consequently, the final average momentum becomes further smaller than the constant L_{ν_e} case.

2.4 Numerical results

First, we show the final spectrum of sterile neutrinos for $m_s = 20$ keV and 50 keV in Fig. 2, where ϵ_{phys} is evaluated as $T = T_* = 1$ MeV. We see that the peak momentum of the final spectrum increases as $L_{\nu_e}^{\text{init}}$ as expected from the analytical discussion in Sec. 2.3.

We also show the time evolution of the lepton asymmetry as a function of the cosmic temperature T in Fig. 3. We see that the lepton asymmetry is consumed around $T = \mathcal{O}(0.1 - 1)$ GeV. Furthermore, the resonance temperature decreases as $L_{\nu_e}^{\text{init}}$ increases and m_s decreases as expected from Eq. (2.23). Note that the quantity $(n_{\nu_s} - n_{\bar{\nu}_s})/s_{\text{tot}} + L_{\nu_e}$ is conserved. Thus, if the resonant production is dominant, the amount of the consumed lepton asymmetry, $\Delta L_{\nu_e} \equiv L_{\nu_e}^{\text{init}} - L_{\nu_e}(T_*)$, satisfies

$$m_s \Delta L_{\nu_e} \simeq \frac{\rho_{\text{DM},0}^{\text{obs}}}{s_{\text{tot},0}}, \quad (2.28)$$

when the sterile neutrino accounts for all dark matter. Thus, the final values of $L_{\nu_e} - L_{\nu_e}^{\text{init}}$ for $L_{\nu_e}^{\text{init}} \geq 10^{-4.5}$ becomes almost the same in Fig. 3. On the other hand, in the case with $L_{\nu_e}^{\text{init}} = 10^{-5}$, the non-resonant production also contributes to the sterile neutrino abundance. Therefore, the final value of $L_{\nu_e} - L_{\nu_e}^{\text{init}}$ for $L_{\nu_e}^{\text{init}} = 10^{-5}$ is different from the other cases.

Finally, we show the contours in the $m_s - \sin^2 2\theta$ plain that explain all dark matter for a given $L_{\nu_e}^{\text{init}}$ in Fig. 4. When $L_{\nu_e}^{\text{init}}$ satisfies the condition

$$m_s L_{\nu_e}^{\text{init}} \lesssim \frac{\rho_{\text{DM},0}^{\text{obs}}}{s_{\text{tot},0}}, \quad (2.29)$$

L_{ν_e} is completely consumed and only sterile neutrinos with low momenta are resonantly produced. After the resonant production stops, sterile neutrinos are further produced non-resonantly. In this case, the same order of θ as in the DW case is required to explain all dark matter since the sterile neutrinos with $\sim \rho_{\text{DM}}^{\text{obs}}$ must be non-resonantly produced. On the other hand, when $L_{\nu_e}^{\text{init}}$ satisfies

$$m_s L_{\nu_e}^{\text{init}} \gtrsim \frac{\rho_{\text{DM},0}^{\text{obs}}}{s_{\text{tot},0}}, \quad (2.30)$$

almost all modes are resonantly produced and the required value of θ becomes significantly smaller than in the DW case. Note that this behavior is different from the contours shown in Refs. [13, 16], in which the contours for non-zero lepton asymmetry begin to deviate from that for the DW case even when m_s is too small to satisfy Eq. (2.30). Although we could not specify the reason for this difference, it might come from the differences in the numerical settings such as the formalization of the mixing angle in the plasma and the assumption on the lepton asymmetry. On the other hand, we obtained the time evolution of the lepton asymmetry for $m_s = 7.1$ keV, $L_{\nu_e}^{\text{init}} \simeq 8 \times 10^{-5}$, and $\sin^2 2\theta = 7 \times 10^{-11}$ consistent with the numerical result in Ref. [19].

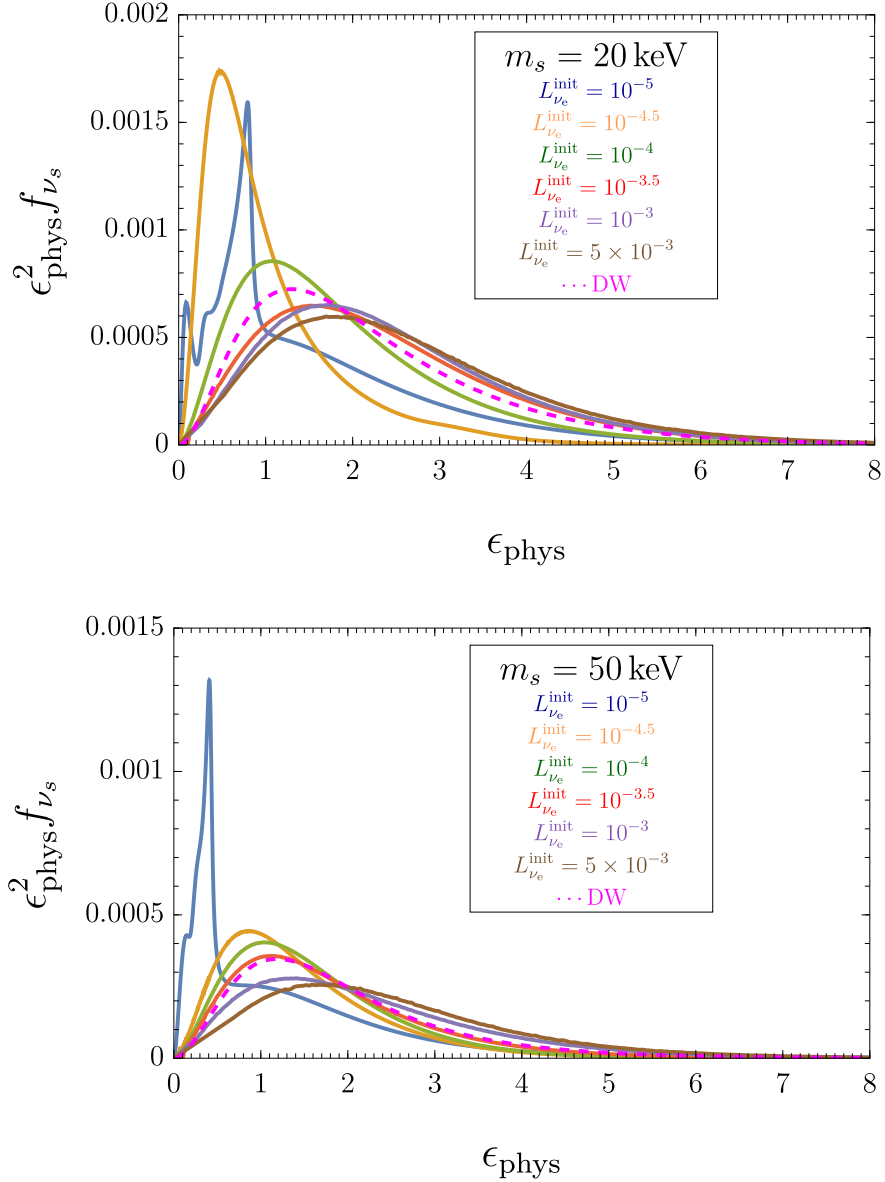


Figure 2. Final spectrum of the sterile neutrino with $m_s = 20$ keV (the upper panel) and $m_s = 50$ keV (the lower panel). ϵ_{phys} is evaluated at $T = 1$ MeV, and the mixing angles are fixed to explain all dark matter for each parameter set. The values of the initial lepton asymmetry are $L_{\nu_e}^{\text{init}} = 10^{-5}, 10^{-4.5}, 10^{-4}, 10^{-3.5}, 10^{-3}, 5 \times 10^{-3}, 0$, respectively. The result for the DW mechanism ($L_{\nu_e}^{\text{init}} = 0$) is shown in the dashed line. $L_{\nu_e}^{\text{init}} = 5 \times 10^{-3}$ corresponds to the center value suggested by Ref. [20].

At the end of this section, we mention other proposed mechanisms for sterile neutrino dark matter production [35, 36]. In the model discussed in Ref. [35], the sterile neutrinos are produced via the decay of gauge singlet Higgs bosons at $T \sim 100$ GeV. In the model discussed in Ref. [36], sterile neutrinos have a gauged $U(1)_{B-L}$ charge, and they are mainly produced from standard model particles in thermal plasma via the $U(1)_{B-L}$ gauge boson exchange. In

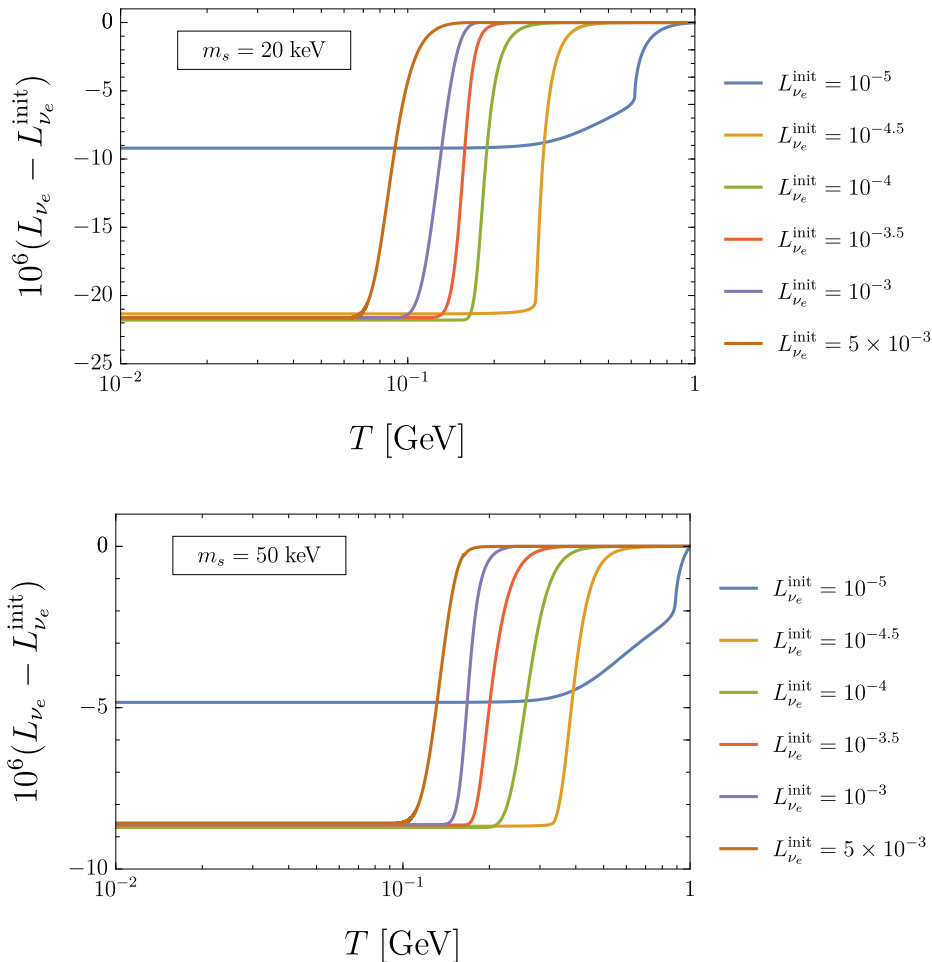


Figure 3. Time evolution of lepton asymmetry with $m_s = 20$ keV (the upper panel) and $m_s = 50$ keV (the lower panel). The values of the initial lepton asymmetry are $L_{\nu_e}^{\text{init}} = 10^{-5}, 10^{-4.5}, 10^{-4}, 10^{-3.5}, 10^{-3}, 5 \times 10^{-3}$, respectively. Mixing angles are fixed to explain all dark matter.

these models, sterile neutrinos are produced at much higher cosmic temperatures than in the resonant production model, and the averaged momentum of dark matter is more redshifted due to the time evolution of g_* . Thus, these scenarios can account for sterile neutrino dark matter with masses of a few keV evading the constraint from the observations of the Lyman- α forests.

2.5 Validity of the stationary point approximation

So far, we have evaluated the production of the sterile neutrino using the stationary point approximation. Here, we discuss the condition to apply the stationary point approximation. When the resonance effect is neglected, Eq. (2.10) gives a solution with $\rho_{a,s}$ oscillating around zero. Since the oscillation period is typically much shorter than the cosmic expansion time scale [27], the right-hand side in Eq. (2.10) is effectively considered to be zero. Thus, we can safely use the stationary point approximation.

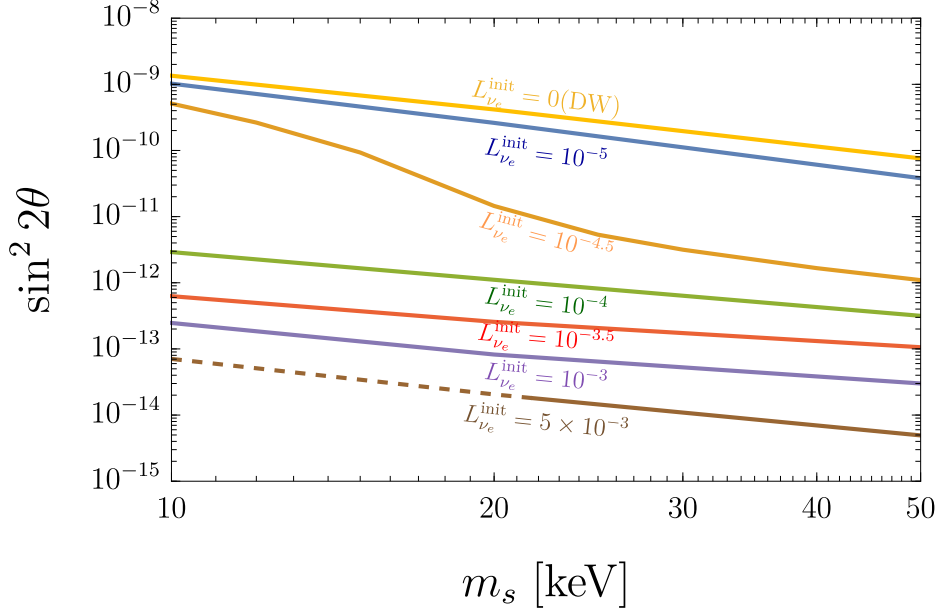


Figure 4. m_s and $\sin^2 2\theta$ to explain all dark matter by the DW and SF mechanisms. The dashed line denotes the parameter region where the stationary point approximation becomes unreliable (see Sec. 2.5).

On the other hand, during the resonance, $\left| \frac{m_s^2}{2p} \cos 2\theta - V_a \right| \ll \Gamma_{\nu_a}$ is satisfied, and Eq. (2.10) is approximately given by

$$i \frac{d}{dt} \rho_{as}(t, \epsilon) \simeq -\frac{m_s^2}{4p} \sin 2\theta \rho_{aa}(t, \epsilon) - i \frac{\Gamma_{\nu_a}}{2} \rho_{as}(t, \epsilon). \quad (2.31)$$

Using $\rho_{aa} \simeq f_{\text{eq}}$, we can approximate that the first term in Eq. (2.31) is time-independent and the solution is given by $\rho_{as} \propto 1 - \exp(-\Gamma_{\nu_a} t/2)$. Then, we regard that the left-hand side of Eq. (2.31) converges to zero in time scale $\sim \Gamma_{\nu_a}^{-1}$. Thus, we consider that if the resonance width δt_{res} satisfies $\delta t_{\text{res}} \gg \Gamma_{\nu_a}^{-1}$, the stationary point approximation can be safely used.

Now let us evaluate the resonance width δt_{res} . The condition for the resonance is given by

$$\left| 1 - \frac{2p}{m_s^2} V_a \right| \lesssim \frac{p}{m_s^2} \Gamma_{\nu_a}. \quad (2.32)$$

Then, the temperature interval satisfying Eq. (2.32), δT_{res} , is given by

$$\frac{\delta T_{\text{res}}}{T_{\text{res}}} \sim \frac{\Gamma_{\nu_a}(T_{\text{res}})}{3V_a(\epsilon_{\text{phys}}, T_{\text{res}})}. \quad (2.33)$$

Therefore, the duration time of resonance δt_{res} is given by

$$\delta t_{\text{res}} \sim \left. \frac{dt}{dT} \right|_{T_{\text{res}}} \times \frac{\Gamma_{\nu_a}(T_{\text{res}}) T_{\text{res}}}{3V_a(\epsilon_{\text{phys}}, T_{\text{res}})}. \quad (2.34)$$

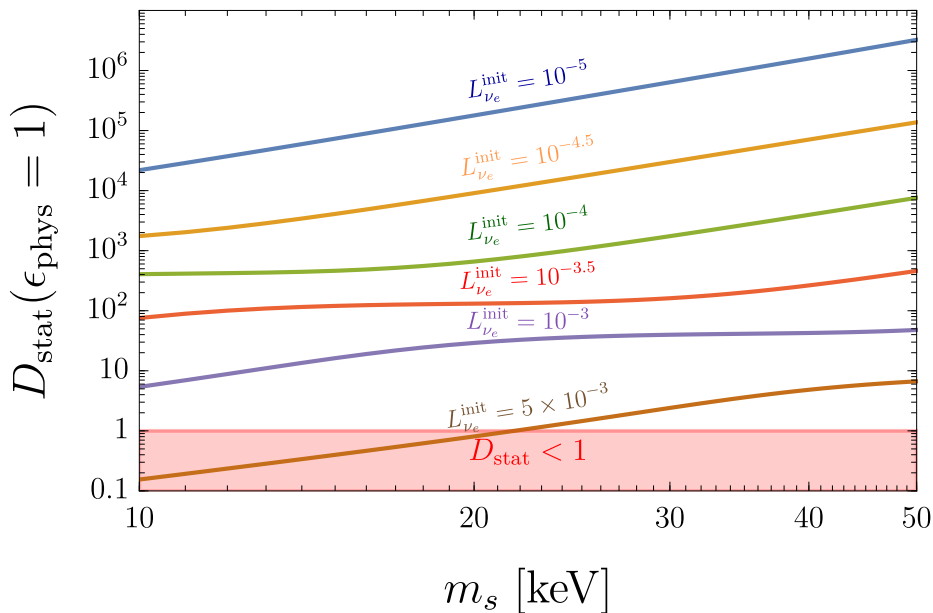


Figure 5. $D_{\text{stat}}(\epsilon_{\text{phys}} = 1)$ defined in Eq. (2.35). For $D_{\text{stat}}(\epsilon_{\text{phys}} = 1) < 1$, the stationary point approximation becomes unreliable.

Here, we regard that the stationary point approximation works if $\delta t_{\text{res}} > \Gamma_{\nu_a}^{-1}$. To quantify the validity of the stationary point approximation, we define

$$D_{\text{stat}} \equiv \left. \frac{dt}{dT} \right|_{T_{\text{low}}} \times \frac{\Gamma_{\nu_a}^2(T_{\text{low}})T_{\text{low}}}{3V_a(\epsilon_{\text{phys}}, T_{\text{low}})}, \quad (2.35)$$

so that the condition to use Eq. (2.14) is given by $D_{\text{stat}} > 1$. Here we evaluate the condition at the lower resonance temperature T_{low} when the sterile neutrino production is dominant. We show D_{stat} as a function of m_s for $\epsilon_{\text{phys}} = 1$ and several values of L_{ν_e} in Fig. 5. We find that the stationary point approximation is valid for $m_s > 10$ keV with $L_{\nu_e} \lesssim 10^{-3}$. On the other hand, it is valid for $m_s \gtrsim 20$ keV in the case with $L_{\nu_e}^{\text{init}} = 5 \times 10^{-3}$.

3 Large lepton asymmetry from Affleck-Dine mechanism

In this section, we discuss the scenario of Affleck-Dine (AD) leptogenesis [37–39] to realize the resonant production of sterile neutrinos.

3.1 Affleck-Dine leptogenesis

AD leptogenesis utilizes flat directions in the scalar potential of the minimal supersymmetric standard model (MSSM). Here, we consider one of the leptonic flat directions and call it the AD field. The potential of the AD field is lifted by supersymmetry (SUSY) breaking effects and the existence of a cutoff at the Planck scale, M_{Pl} .

During inflation, the AD field has a potential given by

$$\begin{aligned} V(\phi) &= m_\phi^2 |\phi|^2 - cH^2 |\phi|^2 + V_{\text{NR}} + V_{\text{A}} \\ &= m_\phi^2 |\phi|^2 - cH^2 |\phi|^2 + |\lambda|^2 \frac{|\phi|^{2(n-1)}}{M_{\text{Pl}}^{2(n-3)}} + \left(\lambda a_M \frac{m_{3/2} \phi^n}{n M_{\text{Pl}}^{n-3}} + \text{h.c.} \right), \end{aligned} \quad (3.1)$$

where m_ϕ is the soft SUSY breaking mass of the AD field, $m_{3/2}$ is the gravitino mass, and c , a_M , and λ are dimensionless constants. In gravity-mediated SUSY breaking models, $m_\phi \sim m_{3/2}$ while m_ϕ is generally much larger than $m_{3/2}$ for gauge-mediated SUSY breaking models.¹ The third term V_{NR} is called the non-renormalizable term, and the fourth term V_{A} is the A-term, which violates a global $U(1)$ symmetry associated with lepton number. $n (\geq 4)$ is an integer depending on the choice of the flat direction and non-renormalizable superpotential. Here, we assume $c = \mathcal{O}(1) > 0$.

After inflation, H decreases and becomes smaller than the SUSY breaking mass at some point. While $H \gtrsim m_\phi$, the AD field has a non-zero field value given by

$$|\phi| \simeq \left(\frac{H M_{\text{Pl}}^{n-3}}{|\lambda|} \right)^{\frac{1}{n-2}}, \quad (3.2)$$

due to the balance between the Hubble-induced mass and the non-renormalizable term. When H becomes comparable to m_ϕ , the origin of the field space is stabilized due to the soft mass term, and the AD field starts to oscillate around the origin. At this period, the field value is given by

$$|\phi| \simeq \varphi_{\text{osc}} \equiv \left(\frac{m_\phi M_{\text{Pl}}^{n-3}}{|\lambda|} \right)^{\frac{1}{n-2}}. \quad (3.3)$$

At the same time, the A-term kicks the AD field in the phase direction. Consequently, the AD field acquires a lepton number proportional to $\varphi^2 \dot{\theta}_{\text{AD}}$, where φ and θ_{AD} are the radial and phase components of ϕ , i.e., $\phi \equiv \varphi e^{i\theta_{\text{AD}}}$. The resulting lepton number density is written as

$$n_L(t_{\text{osc}}) \simeq \delta m_\phi \varphi_{\text{osc}}^2, \quad (3.4)$$

where δ is the efficiency parameter depending on n , the initial phase of the AD field, and the phases of a_M and λ . Notice that δ can take a positive or negative value depending on the initial phase of the AD field.

Now, we comment on the flat direction considered in our scenario. As a concrete flat direction, we consider $\mu^c L_e L_\tau$ or $\tau^c L_e L_\mu$ direction, where a^c is the charge conjugation of an $SU(2)_W$ singlet charged lepton with flavor $a = e, \mu, \tau$, and L_a is an $SU(2)_W$ doublet lepton [40]. As a result, the generated lepton asymmetry satisfies $L_{\nu_e} = -L_{\nu_\mu} = L_{\nu_\tau}$ or $L_{\nu_e} = L_{\nu_\mu} = -L_{\nu_\tau}$, respectively. Then, the first term in the right-hand side in Eq. (2.16) is equal to $2\sqrt{2}G_{\text{F}}L_{\nu_e} s_{\text{tot}}$, which can induce the resonant production of sterile neutrinos.²

¹More precisely, in gauge-mediation models m_ϕ is much larger than $m_{3/2}$ for $|\phi|$ less than the messenger scale. For large field values, the soft SUSY breaking mass term is more complicated and the effective mass decreases with $|\phi|$ until it reaches $m_{3/2}$ as shown in Sec. 3.2.

²On the other hand, $L = 0$ for $e^c L_\mu L_\tau$ flat direction.

3.2 Delayed-type L-ball scenario

From now on, we consider the gauge-mediated SUSY breaking scenario. After the AD field starts to oscillate, the AD field potential is given by

$$V = V_{\text{gauge}} + V_{\text{gravity}} . \quad (3.5)$$

Here, V_{gauge} is the contribution from gauge-mediation given by [41, 42]

$$V_{\text{gauge}} = M_{\text{F}}^4 \left(\ln \frac{|\phi|^2}{M_{\text{S}}^2} \right)^2 , \quad (3.6)$$

where M_{F} is the SUSY breaking scale, and M_{S} is the scale of the messenger sector. Here, we assumed $|\phi| \gg M_{\text{S}}$. V_{gravity} is the contribution from gravity-mediation given by [41, 42]

$$V_{\text{gravity}} = m_{3/2}^2 \left[1 + K \ln \left(\frac{|\phi|^2}{M_{\text{Pl}}^2} \right) \right] |\phi|^2 , \quad (3.7)$$

where K is a dimensionless constant, which we assume to be positive in this paper. We also assume that V_{gravity} is dominant in the potential when the AD field starts to oscillate, i.e., $\varphi_{\text{osc}} > \varphi_{\text{eq}} \equiv M_{\text{F}}^2/m_{3/2}$. When the potential is dominated by V_{gravity} with $K > 0$, the homogeneous oscillation of the AD field is stable. However, right after φ becomes comparable to φ_{eq} , V_{gauge} controls the dynamics of the AD field. In this period, the AD field experiences spatial instabilities and forms spherically symmetric non-topological solitons called L-balls [43–45]. We call this type of L-ball formation scenario “delayed-type” L-ball scenario [46].

Delayed-type L-balls have the same properties as the gauge-mediated type L-balls. Then, the initial charge, mass, radius, and energy per charge of a delayed-type L-ball are given by [45]

$$|Q_{\text{G}}^{\text{init}}| \simeq \beta_{\text{G}} \frac{\varphi_{\text{eq}}^4}{M_{\text{F}}^4} \simeq \beta_{\text{G}} \left(\frac{M_{\text{F}}}{m_{3/2}} \right)^4 , \quad (3.8)$$

$$M_{\text{Q}} \simeq \frac{4\sqrt{2}\pi}{3} \zeta M_{\text{F}} |Q_{\text{G}}|^{\frac{3}{4}} , \quad (3.9)$$

$$R_{\text{Q}} \simeq \frac{1}{\sqrt{2}\zeta} M_{\text{F}}^{-1} |Q_{\text{G}}|^{\frac{1}{4}} , \quad (3.10)$$

$$\omega_{\text{Q}} \simeq \sqrt{2}\pi\zeta M_{\text{F}} |Q_{\text{G}}|^{-\frac{1}{4}} , \quad (3.11)$$

where $\beta_{\text{G}} \simeq 6 \times 10^{-5}$ [47] in the case with $|\delta| \lesssim 10^{-1}$, which we consider in this paper, and ζ is a numerical factor $\simeq 2^{1/4}(c_0/\pi)^{1/2}$ where $c_0 \equiv 4.8 \ln(m_\phi/\sqrt{2}\omega_{\text{Q}}) + 7.4$ [48]. In the following, we adopt $\zeta = 3.4$, which is obtained by substituting $m_{3/2} = 1 \text{ GeV}$, $M_{\text{F}} = 10^6 \text{ GeV}$ and $m_\phi = 10^4 \text{ GeV}$. The L-balls decay into neutrinos with the decay rate Γ_{Q} given by [49, 50]

$$\Gamma_{\text{Q}} \equiv -\frac{1}{Q_{\text{G}}} \frac{dQ_{\text{G}}}{dt} \simeq \frac{N_l}{|Q_{\text{G}}|} \frac{\omega_{\text{Q}}^3}{12\pi^2} 4\pi R_{\text{Q}}^2 \simeq \frac{\sqrt{2}\pi^2 N_l \zeta}{3\beta_{\text{G}}^{5/4}} \frac{m_{3/2}^5}{M_{\text{F}}^4} , \quad (3.12)$$

where $N_l = 3$ is the number of active neutrino species.

To realize the generation of a large lepton asymmetry from L-ball decay, we assume that L-balls dominate the energy density of the universe at L-ball decay. Then, the resulting

lepton-to-entropy ratio from L-ball decay is evaluated as

$$\begin{aligned} L_{\nu_e}^{\text{init}} &\simeq \frac{n_L(t_{\text{osc}})}{m_{3/2}^2 \varphi_{\text{osc}}^2} \frac{\rho_Q(t_{\text{decay}})}{s(t_{\text{decay}})} \\ &\simeq \delta \frac{3T_{\text{decay}}}{4m_{3/2}}, \end{aligned} \quad (3.13)$$

where ρ_Q is the energy density of the L-balls, and T_{decay} is the cosmic temperature just after L-ball decay. L-balls decay almost instantaneously when the decay rate Γ_Q becomes equal to the Hubble parameter. Thus, T_{decay} is given by

$$\begin{aligned} T \simeq T_{\text{decay}} &\equiv \left(\frac{90}{\pi^2 g_*(T_{\text{decay}})} \right)^{1/4} \sqrt{M_{\text{Pl}} \Gamma_Q} \\ &\simeq 2.7 \text{ GeV} \times \left(\frac{g_*}{80} \right)^{-1/4} \left(\frac{m_{3/2}}{1 \text{ GeV}} \right)^{5/2} \left(\frac{M_{\text{F}}}{10^6 \text{ GeV}} \right)^{-2}. \end{aligned} \quad (3.14)$$

Finally, we discuss the condition for L-balls to dominate the universe before the L-ball decay. To this end, we define a ratio f_Q of the energy density of L-balls (or the AD field) ρ_Q to that of the inflaton and inflaton decay products ρ_{R} . Considering that f_Q is almost constant during $t_{\text{osc}} \lesssim t \lesssim t_{\text{R}}$, where t_{R} is the cosmic time at the completion of reheating, and scales as $\propto T^{-1}$ after reheating, we obtain

$$f_Q(T_{\text{decay}}) \simeq \frac{g_*(T_{\text{decay}}) T_{\text{decay}}^4}{g_*(T_{\text{relic,dec}}) T_{\text{relic,dec}}^4} \simeq \frac{m_{3/2}^2 \varphi_{\text{osc}}^2}{3M_{\text{Pl}}^2 H_{\text{osc}}^2} \frac{T_{\text{R}}}{T_{\text{relic,dec}}}, \quad (3.15)$$

where $T_{\text{relic,dec}}$ is the temperature of relic plasma from the inflaton right before the L-ball decay, and T_{R} is the reheating temperature. Then, we obtain

$$f_Q(T_{\text{decay}}) \simeq \left(\frac{g_*(T_{\text{relic,dec}})}{g_*(T_{\text{decay}})} \right)^{1/3} \left(\frac{T_{\text{R}}}{T_{\text{decay}}} \right)^{4/3} \left(\frac{\varphi_{\text{osc}}^2}{3M_{\text{Pl}}^2} \right)^{4/3}. \quad (3.16)$$

Thus, the condition $f_Q(T_{\text{decay}}) > 1$ can be satisfied for a sufficiently large $\varphi_{\text{osc}} (\lesssim M_{\text{Pl}})$ and $T_{\text{R}} > T_{\text{decay}}$.

Now, we search for the compatible parameter space to realize the resonant production of sterile neutrinos. When the decay temperature of L-balls is lower than the resonance temperature of sterile neutrinos, the resonant production does not occur. Therefore, we require $T_{\text{low}} < T_{\text{decay}}$ for ϵ with which the sterile neutrinos are efficiently produced. In the following, we fix $\epsilon_{\text{phys}} = 1$ as a typical value and evaluate T_{low} as a function of the sterile neutrino mass m_s and the initial lepton asymmetry $L_{\nu_e}^{\text{init}}$. We denote the resulting value of T_{low} as $T_{\text{low}}(m_s, L_{\nu_e}^{\text{init}})$. Consequently, the condition for the resonant production is written as

$$T_{\text{low}} \left(m_s, L_{\nu_e}^{\text{init}} = \delta \frac{3T_{\text{decay}}}{4m_{3/2}} \right) < T_{\text{decay}}. \quad (3.17)$$

Using Eqs. (3.14) and (3.17), we obtain the condition that $m_{3/2}$, M_{F} , and m_s should satisfy as

$$\begin{aligned} M_{\text{F}} &\lesssim 3.1 \times 10^6 \text{ GeV} \left(\frac{g_*(T_{\text{decay}})}{80} \right)^{-1/8} \left(\frac{g_*(T_{\text{low}})}{60} \right)^{1/10} \left(\frac{|\delta|}{10^{-3}} \right)^{1/10} \\ &\times \left(\frac{m_{3/2}}{1 \text{ GeV}} \right)^{23/20} \left(\frac{m_s}{50 \text{ keV}} \right)^{-1/5}. \end{aligned} \quad (3.18)$$

Next, we consider the baryon asymmetry produced from the evaporation process of L-balls until the sphaleron process becomes out of equilibrium [51]. The total evaporated baryon charge can be written as [45]³

$$\frac{\Delta Q_b}{Q_G^{\text{init}}} \simeq \begin{cases} -\frac{16\pi}{23\sqrt{5}} \frac{\sqrt{g_*(T_R)}}{g_*(T_{\text{ew}})} \left(32 + 96 \log \frac{T_{\text{eq}}}{T_{\text{ew}}} \right) \frac{M_{\text{Pl}} T_R^2}{\zeta M_s^2 M_{\text{F}}} |Q_G^{\text{init}}|^{-3/4} & (T_R < T_{\text{ew}} < T_{\text{eq}}) \\ -\frac{16\pi}{23\sqrt{5}} \frac{1}{\sqrt{g_*(T_{\text{ew}})}} \left(47 - 15 \frac{T_{\text{ew}}^2}{T_R^2} + 96 \log \frac{T_{\text{eq}}}{T_R} \right) \frac{M_{\text{Pl}} T_R^2}{\zeta M_s^2 M_{\text{F}}} |Q_G^{\text{init}}|^{-3/4} & (T_{\text{ew}} < T_R < T_{\text{eq}}) , \\ -\frac{16\pi}{23\sqrt{5}} \frac{1}{\sqrt{g_*(T_{\text{ew}})}} \left(45 - 15 \frac{T_{\text{ew}}^2}{T_{\text{eq}}^2} + 2 \frac{T_{\text{eq}}}{T_R} \right) \frac{M_{\text{Pl}} T_{\text{eq}}^2}{\zeta M_s^2 M_{\text{F}}} |Q_G^{\text{init}}|^{-3/4} & (T_{\text{ew}} < T_{\text{eq}} < T_R) \end{cases} \quad (3.19)$$

where M_s is the mass of gauginos involved in the evaporation process.

Here, $T_{\text{eq}} \sim (M_s^2 M_{\text{F}})^{1/3} |Q_G^{\text{init}}|^{-1/12}$ is the temperature at which the evaporation rate of L-balls [51] and the diffusion rate of leptons evaporated from L-balls [52] becomes equal, and T_{ew} is the temperature at electroweak phase transition. We assumed $g_*(T) = g_*(T_{\text{ew}})$ for $T > T_{\text{ew}}$. Then, if $T_R < T_{\text{ew}} < T_{\text{eq}}$, the total baryon asymmetry induced from the L-ball evaporation process can be evaluated as

$$\begin{aligned} \eta_b &\simeq \eta_L \left(\frac{\Delta Q_b}{Q_G^{\text{init}}} \right) \\ &\simeq -5.5 \times 10^{-11} \left(\frac{g_*}{80} \right)^{-\frac{1}{4}} \left(\frac{\delta}{10^{-3}} \right) \left(\frac{M_s}{10^4 \text{ GeV}} \right)^{-2} \left(\frac{m_{3/2}}{1 \text{ GeV}} \right)^{\frac{9}{2}} \left(\frac{M_{\text{F}}}{10^6 \text{ GeV}} \right)^{-6} \left(\frac{T_R}{10 \text{ GeV}} \right)^2, \end{aligned} \quad (3.20)$$

where η_L is the lepton-to-entropy ratio and we take $\eta_L = L_{\nu_e}^{\text{init}}$. We require that this resulting baryon asymmetry does not spoil the BBN, that is, $|\eta_b| < |\eta_b^{\text{obs}}| \sim 10^{-10}$, which leads to the upper bound of T_R in terms of M_s , $m_{3/2}$, and M_{F} . On the other hand, the L-ball domination ($f_Q \gg 1$) requires $T_R \gtrsim T_{\text{decay}}$. Thus, using Eq. (3.14) and the upper bound on T_R , we obtain

$$M_{\text{F}} \gtrsim 7.3 \times 10^5 \text{ GeV} \left(\frac{g_*(T_{\text{decay}})}{80} \right)^{-3/40} \left(\frac{|\delta|}{10^{-3}} \right)^{1/10} \left(\frac{m_{3/2}}{1 \text{ GeV}} \right)^{19/20} \left(\frac{M_s}{10^4 \text{ GeV}} \right)^{-1/5}. \quad (3.21)$$

Notice that if $\eta_L < 0$ and $\eta_b \sim 10^{-10}$, the baryon asymmetry produced through the L-ball evaporation can explain the present baryon asymmetry of the universe although negative lepton asymmetry may not be favored by the recent observation of the primordial helium abundance [20].

Finally, we consider the gravitino problem. The gravitino density parameter $\Omega_{3/2}$ is approximately given by [53]

$$\Omega_{3/2} h^2 \simeq 0.71 \left(\frac{m_{3/2}}{0.5 \text{ GeV}} \right)^{-1} \left(\frac{M_{\tilde{g}}}{10^4 \text{ GeV}} \right)^2 \left(\frac{T_R}{10^5 \text{ GeV}} \right) s_Q^{-1}, \quad (3.22)$$

where $M_{\tilde{g}}$ is the gluino mass. Here, we added a factor s_Q , which represents the dilution of gravitinos due to entropy production via L-balls decay and is defined by

$$s_Q \equiv \frac{g_*(T_{\text{decay}}) T_{\text{decay}}^3}{g_*(T_{\text{relic,dec}}) T_{\text{relic,dec}}^3}. \quad (3.23)$$

³Here, we assume $T_{\text{ew}} < T_{\text{eq}}$.

From Eq. (3.15), we obtain

$$s_Q \sim f_Q(T_{\text{decay}})^{3/4}. \quad (3.24)$$

The condition that $\Omega_{3/2} h^2 \ll 0.12$ can be satisfied if we assume sufficiently large $\varphi_{\text{osc}} (\lesssim M_{\text{Pl}})$ in the parameter region of interest. Although gravitinos are also generated from L-ball decay, its contribution is negligibly small compared with the thermal contribution [47].

We show the constraints on $m_{3/2}$ and M_{F} for fixed values of m_s , $|\delta|$, and M_s in Fig. 6. The red region with large $m_{3/2}$ and small M_{F} is excluded by the constraint from $|\eta_b|$ generated via L-ball evaporation process and sphaleron process. On the other hand, the cyan region with small $m_{3/2}$ and large M_{F} is excluded by the requirement that the decay temperature of L-balls should be higher than the resonance temperature of sterile neutrino production. The parameters realizing $|L_{\nu_e}^{\text{init}}| \lesssim 10^{-4}$ is severely constrained by the latter condition because the resonance temperature becomes higher with a lower value of $|L_{\nu_e}^{\text{init}}|$ (see Eq. (2.22)). On the other hand, the parameters realizing $|L_{\nu_e}^{\text{init}}| \gtrsim 10^{-4}$ are allowed in a wide range.

4 Observational implications

In this section, we discuss the observational implications of our scenario.

4.1 Free-streaming length of sterile neutrinos

Here, we discuss the free streaming of the produced sterile neutrinos. From the observations of the Lyman- α forests in the quasar spectra, the free streaming of dark matter can be constrained. This constraint is highly dependent on the final spectrum of sterile neutrinos. Here, we obtain a constraint on the mass of sterile neutrinos with the vacuum mixing angle θ fixed to explain all dark matter. This constraint is discussed in detail by Ref. [13]. However, as we mentioned in Sec. 2.4, our relation among θ , m_s , and $L_{\nu_e}^{\text{init}}$ to explain all dark matter is different from one used in Ref. [13]. Thus, we revisit the constraint here. In deriving the constraint, we first use the Lyman- α constraint on the mass of early decoupled thermal relics [54] and translate it into the upper bound of the free-streaming length $\lambda_{\text{FS}}^{\text{upper}}$ of dark matter. We then estimate the free-streaming lengths from the final spectra obtained in Sec. 2 and compare them to $\lambda_{\text{FS}}^{\text{upper}}$. Finally, we obtain the lower bound on m_s for each value of $L_{\nu_e}^{\text{init}}$ in a similar way to Ref. [29].

The typical free-streaming length of particles decoupled from the thermal plasma is given by [13]

$$\lambda_{\text{FS}} \simeq a(t) \int_{a_{\text{in}}}^{a(t)} da \frac{v(\langle \epsilon \rangle, t)}{a(t)^2 H(t)}, \quad (4.1)$$

where $\langle \epsilon \rangle$ is ϵ averaged over the momentum distribution at $T = T_{\text{in}}$, which is the lower one of the decoupling temperature and the particle production temperature, and a_{in} is the scale factor at $T = T_{\text{in}}$.

We evaluate the free-streaming length of early decoupled thermal relics as a function of the relic mass m_x . Here, an early decoupled thermal relic follows the Fermi-Dirac distribution given by

$$f_X(p) = \frac{1}{1 + \exp(p/T_x)}, \quad (4.2)$$

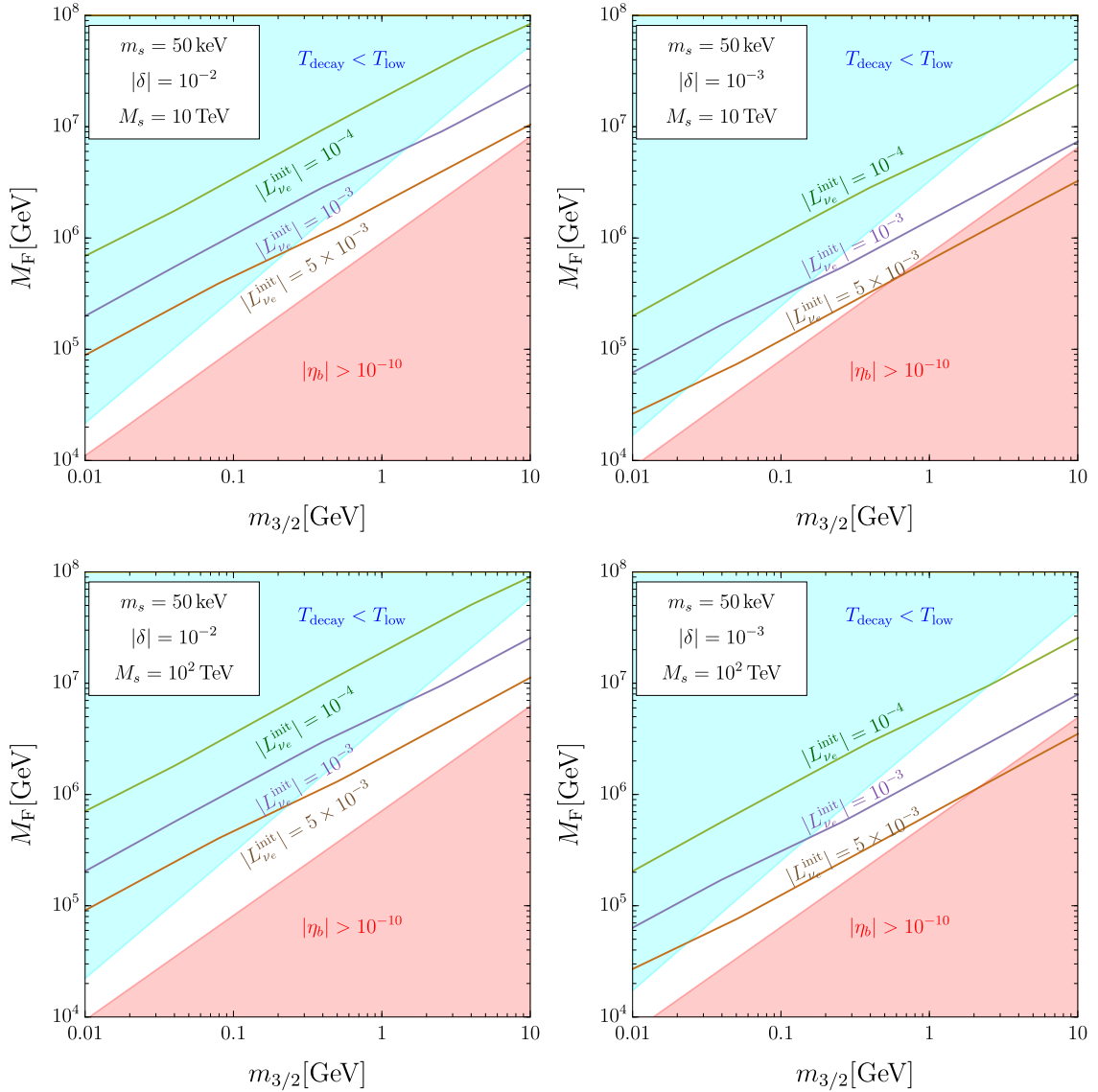


Figure 6. Constraints on $m_{3/2}$ and M_F in the delayed-type L-ball scenario. We set $M_s = 10$ TeV in the upper panels and $M_s = 10^2$ TeV in the lower panels. We set $\delta = 10^{-2}$ and $\delta = 10^{-3}$ in the left and right panels, respectively. The green, violet, and brown lines correspond to $|L_{\nu_e}^{\text{init}}| = 10^{-4}$, 10^{-3} , and 5×10^{-3} , respectively. The red-shaded region is excluded because baryon asymmetry is overproduced, $|\eta_b| > 10^{-10}$, due to the evaporation process of L-balls when we require $T_R > T_{\text{decay}}$ (see Eq. (3.21)). The cyan region is excluded because T_{decay} is lower than T_{low} (see Eq. (3.18)).

where T_x is the temperature of the thermal relic, and its energy density is equal to $\rho_{\text{DM}}^{\text{obs}}$. Therefore, the relation between m_x and T_x after neutrino decoupling is given by [14, 29, 54]

$$\frac{m_{\text{eff}}}{m_x} = \left(\frac{T_x}{T_\nu} \right)^3, \quad (4.3)$$

where $m_{\text{eff}} = 94 \text{ eV} \times \Omega_{\text{DM}} h^2$ is the total mass of the active neutrinos for their energy density to be the same as dark matter, and T_ν is the temperature of active neutrinos. Using the

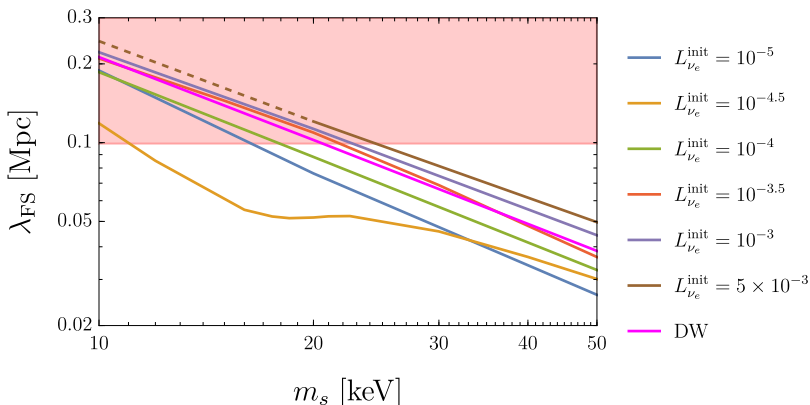


Figure 7. Free-streaming length of sterile neutrinos λ_{FS} as a function of m_s . The red-shaded region is constrained by the Lyman- α forest observations.

relation between m_x and λ_{FS} , we translate the lower bound, $m_x > 4.09$ keV (95% CL) [54], into the upper bound of λ_{FS} , $\lambda_{\text{FS}} < \lambda_{\text{FS}}^{\text{upper}} = 0.099$ Mpc.

In the case of the sterile neutrino, we take $T_{\text{in}} = T_*$ because the free-streaming length until $T = T_*$ is negligible. The velocity $v(t)$ is given by

$$v = \frac{p}{\sqrt{p^2 + m_s^2}} = \frac{\epsilon_{\text{phys}}(T_*)}{\sqrt{\epsilon_{\text{phys}}(T_*)^2 + \left(\frac{m_s}{T_*}\right)^2 \left(\frac{a}{a_*}\right)^2}}, \quad (4.4)$$

where we used $p = \epsilon_{\text{phys}}(T_*)T_*a_*/a$. Now, we calculate the free-streaming length of the sterile neutrinos in the SF mechanism using the distribution function obtained in Sec. 2. We show the free-streaming length of the sterile neutrinos as a function of m_s for a given $L_{\nu_e}^{\text{init}}$ in Fig. 7. By equating $\lambda_{\text{FS}}(m_s, L_{\nu_e}^{\text{init}})$ and $\lambda_{\text{FS}}^{\text{upper}} = 0.099$ Mpc, we obtain the Lyman- α constraint on m_s for a given $L_{\nu_e}^{\text{init}}$. We show the lower bounds of m_s for several values of $L_{\nu_e}^{\text{init}}$ in Table 1.

$L_{\nu_e}^{\text{init}}$	0 (DW)	10^{-5}	$10^{-4.5}$	10^{-4}	$10^{-3.5}$	10^{-3}	5×10^{-3}
m_s^{lower} [keV]	21	16	11	18	22	23	24

Table 1. Lyman- α constraints on sterile neutrino mass for given values of $L_{\nu_e}^{\text{init}}$.

The constraint on m_s becomes weaker for $L_{\nu_e}^{\text{init}} \lesssim 10^{-4.5}$ and stronger for $L_{\nu_e}^{\text{init}} \gtrsim 10^{-4.5}$ as $L_{\nu_e}^{\text{init}}$ increases. This trend can be understood as a combination of two effects. First, as discussed in Sec. 2.3, the averaged momentum of resonantly produced sterile neutrinos becomes smaller than the thermal distribution at production. In particular, this effect is significant if the substantial fraction of $L_{\nu_e}^{\text{init}}$ is consumed in the resonant production. Second, the resonance temperature depends on lepton asymmetry as $T_{\text{low}} \propto L_{\nu_e}^{-1/4}$ (see Eq. (2.23)). Thus, larger $L_{\nu_e}^{\text{init}}$ results in later production of sterile neutrinos, which are less red-shifted. Consequently, in spite of the first effect, the averaged momentum of sterile neutrinos for large $L_{\nu_e}^{\text{init}}$ can be larger than that in the DW mechanism when compared at the same temperature. Due to the balance between these effects, the Lyman- α constraint becomes weakest for $L_{\nu_e}^{\text{init}} \simeq 10^{-4.5}$.

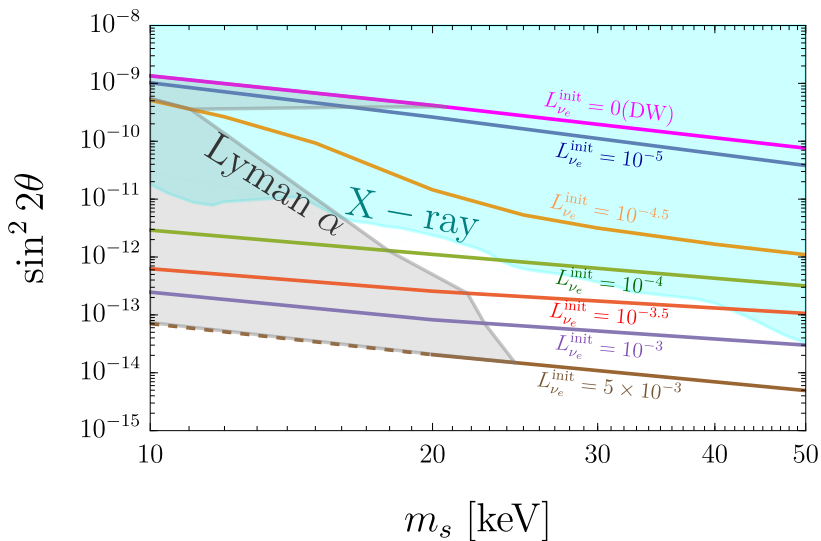


Figure 8. m_s and $\sin^2 2\theta$ to explain all dark matter with the Lyman- α constraint (gray) and the X-ray constraint (light blue). We adopted the conservative X-ray constraint from Ref. [1], which is based on the *NuStar* observations [55].

We show the $m_s - \sin^2 2\theta$ contour to explain all dark matter and observational constraints in Fig. 8. We see that $L_{\nu_e}^{\text{init}} \gtrsim \mathcal{O}(10^{-4})$ is required to evade the current X-ray constraint, and $m_s \gtrsim 20$ keV is required to evade the current Lyman- α constraint.

4.2 Gravitational wave enhancement at L-ball decay

In our scenario, the energy density of L-balls dominates the universe before the L-ball decay. Then, at the L-ball decay, the universe undergoes a sudden transition from the early matter-dominated (eMD) era to the radiation-dominated (RD) era. During the eMD era, the subhorizon mode of the gravitational potential is almost constant and does not decay in contrast to in the RD era. Then, at the sudden transition to the RD era, the gravitational potential begins to oscillate due to radiation pressure. This process induces a large value of the fluid velocity and enhances the scalar-induced gravitational waves. This mechanism of an enhancement of scalar-induced gravitational waves is called ‘‘Poltergeist’’ mechanism [56] and has been studied in the context of the L-ball decay [57–59]. Here, we evaluate the gravitational wave spectrum in our scenario and discuss the testability in future observations.

In the following, we introduce a conformal time $\eta \equiv \int dt/a(t)$. We denote η at the completion of reheating by η_R , η when the energy density of L-balls begins to dominate the universe by $\eta_{\text{eq},1}$, η when the gravitational potential Φ begins to decouple from the matter density perturbation δ_m by $\eta_{\text{eq},2}$, and η at the L-ball decay by η_{decay} .

The approximate analytic study gives the density parameter of gravitational waves per $\ln k$, Ω_{GW} , as [56, 58]⁴

$$\Omega_{\text{GW}}(\eta_c, k) \simeq 2.9 \times 10^{-7} Y \mathcal{P}_\zeta^2 \Phi_{\text{low}}^4(k) (k \eta_{\text{decay}})^7 F(n_{\text{s,eff}}), \quad (4.5)$$

⁴The production of gravitational waves by this mechanism is also studied numerically in Ref. [60].

where Ω_{GW} is defined by

$$\begin{aligned}\Omega_{\text{GW}}(\eta, k) &\equiv \frac{\rho_{\text{GW}}(\eta, k)}{\rho_{\text{tot}}(\eta)} \\ &= \frac{1}{24} \left(\frac{k}{\mathcal{H}(\eta)} \right)^2 \overline{\mathcal{P}_h(\eta, k)}.\end{aligned}\quad (4.6)$$

For details on this formula, see Appendix D. Here, $\rho_{\text{tot}}(\eta)$ is the total energy density at η , $\rho_{\text{GW}}(\eta, k)$ is the energy density of gravitational waves per $\ln k$, $\overline{\mathcal{P}_h(\eta, k)}$ is the time average of the gravitational wave spectrum, and $\mathcal{H} \equiv aH$ is the conformal Hubble parameter. We evaluated the spectrum at a certain time $\eta = \eta_c$ after the production of the gravitational waves and before the late time matter-radiation equality. In Eq. (4.5), $Y \simeq 2.3$ is a numerical fudge factor, and $F(n_{\text{s,eff}})$ is defined using a hypergeometric function ${}_2F_1$ as

$$\begin{aligned}F(n_{\text{s,eff}}) &\equiv 2 \left(\frac{3}{4} \right)^{n_{\text{s,eff}}-1} \\ &\times \left[{}_4F_1 \left(\frac{1}{2}, 1 - n_{\text{s,eff}}; \frac{3}{2}; \frac{1}{3} \right) - {}_3F_1 \left(\frac{1}{2}, -n_{\text{s,eff}}; \frac{3}{2}; \frac{1}{3} \right) - {}_2F_1 \left(\frac{3}{2}, -n_{\text{s,eff}}; \frac{5}{2}; \frac{1}{3} \right) \right],\end{aligned}\quad (4.7)$$

where $n_{\text{s,eff}}$ represents the effective spectral index of Φ_{low} , defined by

$$n_{\text{s,eff}} \equiv 1 + 2 \frac{d \ln \Phi_{\text{low}}}{d \ln k}.\quad (4.8)$$

Here, Φ_{low} is the lower bound of Φ at the onset of RD era and is given by Eq. (D.15). \mathcal{P}_ζ is the power spectrum of the curvature perturbations, and we assume that it is given by the scale-invariant spectrum as

$$\mathcal{P}_\zeta(k) = C^2 A_s,\quad (4.9)$$

where $A_s = 2.1 \times 10^{-9}$ is the amplitude on the CMB pivot scale $k_* = 0.05 \text{ Mpc}^{-1}$ [61], and a constant C is introduced because the amplitude can be much larger at small scales. We translate $\Omega_{\text{GW}}(\eta_c, k)$ into the current value of the gravitational wave energy density parameter as

$$\Omega_{\text{GW},0} h^2 = 0.83 \left(\frac{g_{*,c}}{10.75} \right)^{-1/3} \Omega_{\text{r},0} h^2 \Omega_{\text{GW}}(\eta_c, k),\quad (4.10)$$

which depends on three parameters: C , $\eta_{\text{eq},1}$, and η_{decay} . In other words, the gravitational wave spectrum depends on the amplitude of the scalar perturbations, the decay time of the L-balls, and the duration of the eMD era.

To quantify $\eta_{\text{eq},1}/\eta_{\text{decay}}$ as a function of the parameters on the L-ball scenario, we use the relation between the scale factor and η with $\eta_{\text{eq},1} \lesssim \eta \lesssim \eta_{\text{decay}}$:

$$\frac{a(\eta)}{a(\eta_{\text{eq},1})} = \left(\frac{\eta}{\eta_*} \right)^2 + \frac{2\eta}{\eta_*} \simeq \left(\frac{\eta}{\eta_*} \right)^2,\quad (4.11)$$

where $\eta_* \equiv \eta_{\text{eq},1}/(\sqrt{2}-1)$. In the last equality, we assumed $\frac{a(\eta)}{a(\eta_{\text{eq},1})} \gg 1$. Using Eqs. (3.14), (3.16), and (4.11), we obtain $\eta_{\text{decay}}/\eta_{\text{eq},1}$ as a function of the basic parameters, $m_{3/2}$, M_{F} , T_{R} , and φ_{osc} .

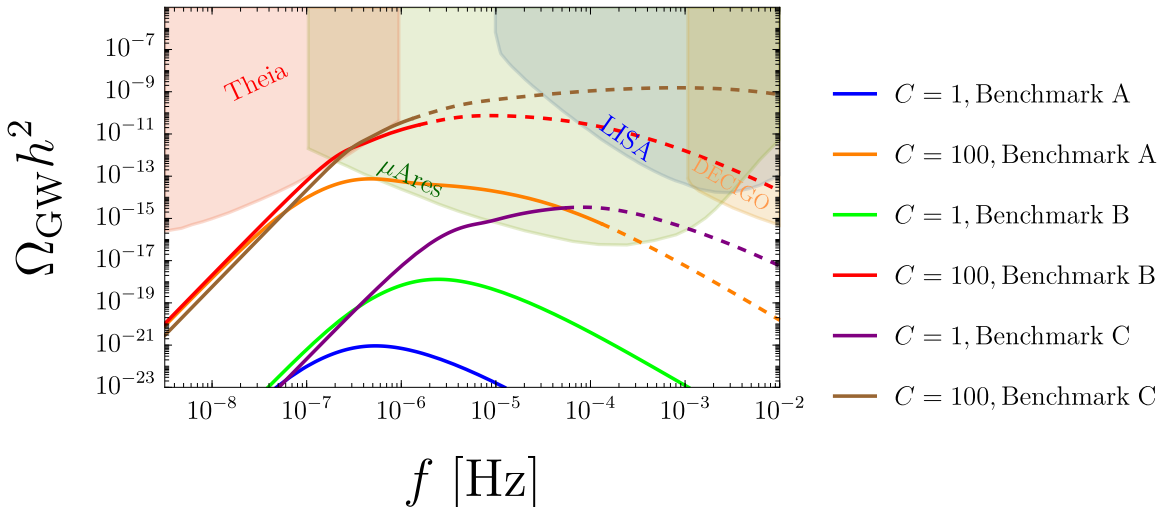


Figure 9. Gravitational wave spectra enhanced at the L-ball decay. The analytic formula becomes unreliable in the dashed regions because the fitting formula (D.9) of non-linear density perturbations in the eMD era may not be applicable in the wavelength corresponding to these regions.

We evaluated the final gravitational wave spectrum with three benchmark parameters shown in Table 2. In these parameter sets, we fixed $\varphi_{\text{osc}}/M_{\text{Pl}} = 0.3$ and $|\delta| = 10^{-3}$. We show the results in Fig. 9. We see that the gravitational waves in cases A and B with $C = 100$, and C with $C = 1, 100$ are detectable in future gravitational wave observations such as μ Ares [24] and THEIA [25]. Moreover, the gravitational wave abundance increases in the order of cases C, B, and A for the same value of C . This is because of the difference in T_{R} . If the reheating temperature is low and near the decay temperature of L-balls (case A), the L-ball domination era lasts for a short period, and the gravitational wave spectrum is not enhanced due to the suppression of subhorizon modes of the scalar perturbations during the eRD era. On the other hand, for $T_{\text{R}} \sim \mathcal{O}(10^4 - 10^5) \text{ GeV} \gg T_{\text{decay}}$, the eMD era lasts long, and the gravitational wave spectrum is significantly enhanced. Note also that a large gaugino mass $M_s \gtrsim \mathcal{O}(10^5) \text{ GeV}$ is assumed in cases B and C. This is because the baryon asymmetry is overproduced due to a large evaporation rate of L-balls for a higher value of T_{R} , unless we assume a large gaugino mass. Note that we fixed M_s in each case so that the baryon asymmetry of the universe $\eta_b^{\text{obs}} \sim 10^{-10}$ can be explained by the L-ball evaporation process and sphaleron process above the electroweak scale.

Finally, we note that our scenario assumes larger values of T_{decay} than Ref. [58], to realize the SF mechanism. Consequently, we obtain enhanced gravitational waves in a higher

	$m_{3/2}$ [GeV]	M_{F} [GeV]	T_{R} [GeV]	M_s [GeV]	$ \eta_{\text{b}} $	$ L_{\nu_e}^{\text{init}} $
A	0.5	1.1×10^6	1.0×10^2	1.5×10^4	8.7×10^{-11}	7.0×10^{-4}
B	0.4	8.5×10^5	1.0×10^3	1.7×10^5	8.7×10^{-11}	8.4×10^{-4}
C	2.0	5.4×10^6	1.4×10^4	2.1×10^5	8.7×10^{-11}	2.2×10^{-4}

Table 2. Benchmark parameters to evaluate the gravitational wave spectra.

frequency region compared with Ref. [58].

5 Conclusion

In this paper, we have investigated the possibility that a large lepton asymmetry generated from L-ball decay induces resonant production of sterile neutrino dark matter. We revisited the numerical calculation of the SF mechanism. As a result, we found that the value of the vacuum mixing angle θ to explain all dark matter largely deviates from the DW case for $L_{\nu_e}^{\text{init}} > \mathcal{O}(10^{-4})$ in the case of $m_s > 10 \text{ keV}$.

We then discussed the AD leptogenesis scenario with the L-ball decay, which produces a large lepton asymmetry in the active neutrino sector as a source of sterile neutrino production. Considering the delayed-type L-balls, we found consistent parameter regions for which sterile neutrinos are resonantly produced through the SF mechanism and account for all the dark matter of the universe.

Finally, we discussed the observational implications of our scenario. We evaluated the free-streaming length of the produced sterile neutrinos from the distribution functions obtained in the numerical calculation. As a result, it was found that the sterile neutrino mass should be $m_s \gtrsim 10 - 20 \text{ keV}$ to be consistent with the current Lyman- α constraint. We also found that the constraint on m_s becomes weaker with larger $L_{\nu_e}^{\text{init}}$ for $L_{\nu_e}^{\text{init}} \lesssim 10^{-4.5}$ while the constraint becomes stronger with larger $L_{\nu_e}^{\text{init}}$ for $L_{\nu_e}^{\text{init}} \gtrsim 10^{-4.5}$. We also discussed the scalar-induced gravitational waves enhanced at the L-ball decay. We found that our scenario is testable in future gravitational wave observations such as μAres and THEIA. However, to discuss the testability of higher frequency modes, $f \gtrsim \mathcal{O}(10^{-5}) \text{ Hz}$, where LISA and DECIGO have good sensitivity, further discussion on the effect of non-linear density evolution on the gravitational potential during the Q-ball dominated era is required.

Acknowledgments

This work was supported by JSPS KAKENHI Grant Nos. 20H05851(M.K.), 21K03567(M.K.), 23KJ0088 (K.M.), and JST SPRING (grant number: JPMJSP2108) (K.K.). K.K. was supported by the Spring GX program.

A Fitting function for y_e

To numerically solve the master equation (2.14), we should take into account the temperature dependence of $y_e(\epsilon, T)$. In this paper, we use a function fitted to the numerical result given in Refs. [32, 33]. For simplicity, we approximate that y_e does not depend on ϵ_{phys} and use the data for $\epsilon_{\text{phys}}(T) = 3$ in Ref. [33]. The fitting formula is given by

$$y_e(\epsilon, T) = \sum_{i=1}^4 \exp \left[c_1^i + c_2^i \left(1 + \tanh \left(\frac{\log \left(\frac{T}{1 \text{ GeV}} \right) + c_3^i}{c_4^i} \right) \right) \right], \quad (\text{A.1})$$

where the values of c_i^j are shown in Table 3. We compare the formula (A.1) with the numerical result in Ref. [33] in Fig. 10.

We note that the value of y_e does not affect the final result in the limit where the time evolution of the lepton asymmetry is negligible during the production of a single mode as we can see that Eq. (2.25) is independent of y_e . On the other hand, if the lepton asymmetry non-negligibly evolves during the resonance of a single mode with fixed ϵ , y_e slightly affects the final distribution of the sterile neutrino.

i	c_1^i	c_2^i	c_3^i	c_4^i
1	-0.848259	0.685952	1.76853	0.174619
2	-2.36415	1.55878	1.2981	0.656795
3	-1.52151	1.50891	1.64656	1.5446
4	-0.792215	0.464922	3.63313	0.572627

Table 3. Fitting parameters for y_e , c_j^i ($i, j = 1, \dots, 4$).

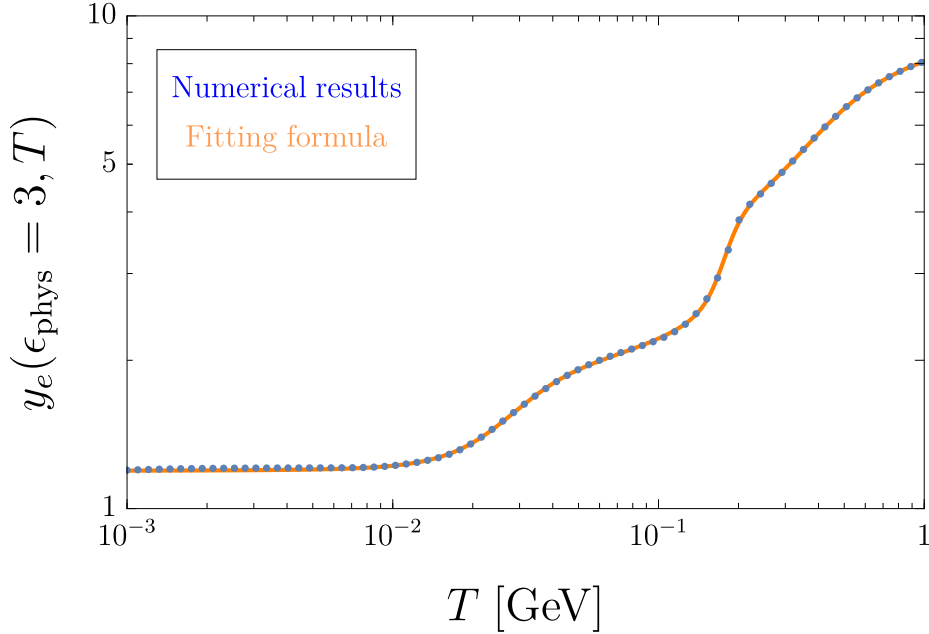


Figure 10. Fitting formula (A.1) for y_e used in this paper (orange line) and the numerical results presented in Ref. [33] (blue dots).

B Numerical dependence on the number of bins used in momentum space

To solve Eqs. (2.14) and (2.19) simultaneously, we discretize the momentum space as $\epsilon = \epsilon_{\max}/N_{\text{bin}} \times i$, where N_{bin} is the number of momentum bins, $i = 1, \dots, N_{\text{bin}}$, and ϵ_{\max} is the maximum value of ϵ in the numerical calculation. Here, we fix $\epsilon_{\max} = 20$ and observe the dependence of the final abundance Ω_{ν_s} on N_{bin} .

We show the dependence of the sterile neutrino abundance Ω_{ν_s} on N_{bin} with fixed θ in Fig. 11. Here, we chose θ to realize $|\Omega_{\nu_s}/\Omega_{\text{DM}} - 1| < \mathcal{O}(10^{-3})$ with the value of N_{bin} used in Sec. 2 ($= N_{\text{bin}}^{\text{max}}$). We summarize the values of $N_{\text{bin}}^{\text{max}}$ in Table. 4. Note that $N_{\text{bin}}^{\text{max}}$ does not depend on m_s . These are the maximum values due to the limitation of the performance of our computer memories. From Fig. 11, we see that the dependence on N_{bin} is insignificant at $N_{\text{bin}} = N_{\text{bin}}^{\text{max}}$ with $L_{\nu_e}^{\text{init}} \lesssim 10^{-4}$. On the other hand, with $L_{\nu_e} \gtrsim 10^{-3.5}$, Ω_{ν_s} still increases at $N_{\text{bin}} = N_{\text{bin}}^{\text{max}}$.

The reason can be qualitatively understood as follows. If L_{ν_e} decreases significantly during a resonant production of a single mode ϵ , the resonance terminates earlier because T_{low} grows as $T_{\text{low}} \propto L_{\nu_e}^{-1/4}$. If we use large $\Delta\epsilon$, the decrease of L_{ν_e} during the resonance of a given

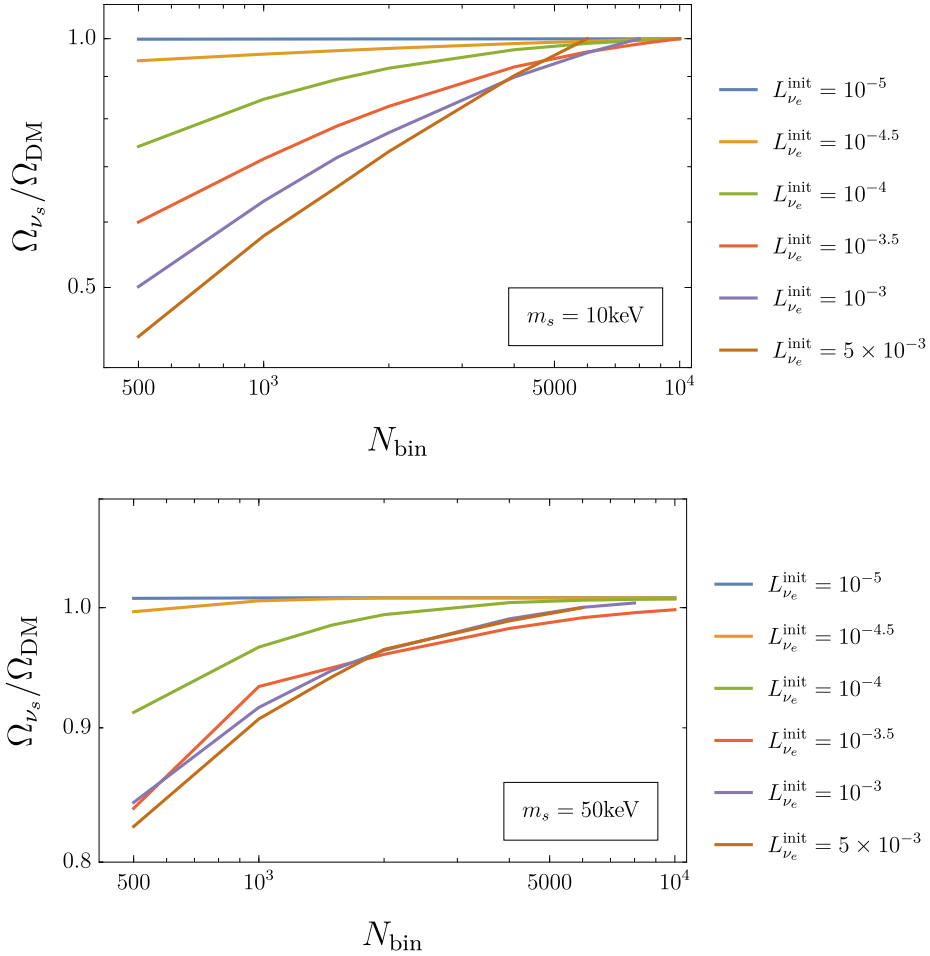


Figure 11. Dependence of the sterile neutrino abundance Ω_{ν_s} on N_{bin} with fixed θ .

ϵ is overestimated, and thus the resonant production of sterile neutrinos is underestimated. Thus, the estimation with constant L_{ν_e} gives an upper bound on the final abundance. For instance, with $m_s = 10 \text{ keV}$ and $L_{\nu_e}^{\text{init}} = 5 \times 10^{-3}$ (the case in which the final spectrum dependence on N_{bin} is the strongest), the final abundance becomes $\Omega_{\nu_s}/\Omega_{\text{DM}} = 1.46$ with the same θ as in the contour in Fig. 4, assuming that L_{ν_e} is constant. Thus, we conclude that at least our estimation has an accuracy of several tens of percent.

C Analytical estimate of the sterile neutrino spectrum

Here, we show the derivation of the analytical estimate of the sterile neutrino spectrum in Sec. 2.3. If the sterile neutrinos are produced mainly via the SF mechanism, the contribution

$L_{\nu_e}^{\text{init}}$	10^{-5}	$10^{-4.5}$	10^{-4}	$10^{-3.5}$	10^{-3}	5×10^{-3}
$N_{\text{bin}}^{\text{max}}$	10^4	10^4	10^4	10^4	8000	6000

Table 4. $N_{\text{bin}}^{\text{max}}$ used in the numerical studies in Sec. 2.

of anti-neutrinos is negligible, and the time evolution of f_{ν_s} is described by

$$\frac{d}{dT} f_{\nu_s}(\epsilon, T) \simeq \frac{dt}{dT} \Gamma_{\nu_a}(\epsilon, T) \theta_M^2(\epsilon, T) f_{\nu_e}(\epsilon, T). \quad (\text{C.1})$$

Now, we integrate the right-hand side over T . Since most of the sterile neutrinos are produced around $T = T_{\text{low}}$, we focus on $T \sim T_{\text{low}}$. Then, θ_M is approximately given as

$$\begin{aligned} \theta_M^2 &= \theta^2 \left[\left(1 - \frac{2p}{m_s^2} V_a(\epsilon, T) \right)^2 + \frac{p^2 \Gamma_{\nu_a}^2(\epsilon, T)}{m_s^4} \right]^{-1} \\ &\simeq \theta^2 [x(\epsilon, T)^2 + y(\epsilon, T)^2]^{-1}, \end{aligned} \quad (\text{C.2})$$

where

$$x(\epsilon, T) \equiv 1 - \frac{8\sqrt{2}\pi^2 G_F \epsilon_{\text{phys}}(T) L_{\nu_e} g_*(T) T^4}{45m_s^2}, \quad (\text{C.3})$$

$$y(\epsilon, T) \equiv \frac{\epsilon_{\text{phys}}(T) \Gamma_{\nu_a}(\epsilon, T) T}{m_s^2}. \quad (\text{C.4})$$

Here, we assume that the time evolution of L_{ν_e} is negligible, and then x is a monotonically decreasing function of T . As a result, we can integrate Eq. (C.1) with respect to x and obtain

$$f_{\nu_s} \simeq \int_{x_{\text{min}}}^{x_{\text{max}}} dx \left| \frac{dT}{dx} \frac{dt}{dT} \right| \frac{\theta^2 f_{\nu_e}(\epsilon, T) \Gamma_{\nu_a}(\epsilon, T)}{x^2 + y(\epsilon, T)^2}, \quad (\text{C.5})$$

where x_{min} and x_{max} denote the integration range of Eq. (C.1). Since the resonance occurs at $x \simeq 0$, the contribution to f_{ν_s} mainly comes from the integration around $x = 0$, which corresponds to $T = T_{\text{low}}$. Thus, we neglect the temperature dependence of the integrand except for the resonant part and obtain

$$f_{\nu_s} \simeq \left| \frac{dT}{dx} \right|_{T_{\text{low}}} \left| \frac{dt}{dT} \right|_{T_{\text{low}}} \theta^2 \Gamma_{\nu_a}(\epsilon, T_{\text{low}}) f_{\nu_e}(\epsilon, T_{\text{low}}) \int_{x_{\text{min}}}^{x_{\text{max}}} \frac{dx}{x^2 + y(\epsilon, T_{\text{low}})^2}. \quad (\text{C.6})$$

Due to the resonant feature of the integrand, we can approximately set $x_{\text{min}} = -\infty$ and $x_{\text{max}} = \infty$. Consequently, we obtain

$$\begin{aligned} f_{\nu_s} &\simeq \left| \frac{dT}{dx} \right|_{T_{\text{low}}} \left| \frac{dt}{dT} \right|_{T_{\text{low}}} \theta^2 \Gamma_{\nu_a}(\epsilon, T_{\text{low}}) f_{\nu_e}(\epsilon, T_{\text{low}}) \frac{\pi}{y(\epsilon, T_{\text{low}})} \\ &= \frac{135\sqrt{5}}{32\pi^2} \frac{g_*^{2/3}(T_i)}{g_*^{13/6}(T_{\text{low}})} \frac{M_{\text{Pl}} m_s^4 \theta^2}{G_F \epsilon^2 T_{\text{low}}^7} \frac{f_{\nu_e}(\epsilon, T_{\text{low}})}{L_{\nu_e}(T_{\text{low}})}. \end{aligned} \quad (\text{C.7})$$

In a similar way, we also obtain the contribution from the resonance at T_{high} as

$$f_{\nu_s} \simeq \frac{135\sqrt{5}}{16\pi^2} \frac{g_*^{2/3}(T_i)}{g_*^{13/6}(T_{\text{high}})} \frac{1 + \frac{1}{3} \frac{d \ln g_*}{d \ln T}(T_{\text{high}})}{1 - \frac{1}{3} \frac{d \ln g_*}{d \ln T}(T_{\text{high}})} \frac{M_{\text{Pl}} m_s^4 \theta^2}{G_F \epsilon^2 T_{\text{high}}^7} \frac{f_{\nu_e}(\epsilon, T_{\text{high}})}{L_{\nu_e}(T_{\text{high}})}. \quad (\text{C.8})$$

Note that the factor $(1 + \frac{1}{3} \frac{d \ln g_*}{d \ln T}(T_{\text{high}})) / (1 - \frac{1}{3} \frac{d \ln g_*}{d \ln T}(T_{\text{high}})) \simeq 1$ is omitted in Eq. (2.26). This approximation becomes less accurate for a smaller value of m_s , fixing the final abundance of sterile neutrinos. This is because we cannot regard L_{ν_e} as constant during the resonance of a single mode ϵ .

D Review of gravitational waves enhanced at the L-ball decay

In this appendix, we briefly review the basic formalism to evaluate the gravitational wave spectrum enhanced at the L-ball decay based on Refs. [56–58]. Here, we use the conformal Newtonian gauge. Then, the metric perturbation is given by

$$ds^2 = a^2 \left[-(1 + 2\Phi)d\eta^2 + \left((1 - 2\Psi)\delta_{ij} + \frac{1}{2}h_{ij} \right) dx^i dx^j \right], \quad (\text{D.1})$$

where Φ and Ψ is the first-order scalar perturbations, and h_{ij} is the tensor perturbation. In the following, we neglect the anisotropic stress and take $\Phi = \Psi$.

Now, we discuss the second-order tensor perturbation h_{ij} induced by the first-order scalar perturbation Φ . The time-averaged gravitational wave spectrum $\overline{\mathcal{P}_h(\eta, k)}$ induced by the first-order scalar perturbations is given by [62–64]

$$\overline{\mathcal{P}_h(\eta, k)} = 4 \int_0^\infty dv \int_{|1-v|}^{1+v} du \left(\frac{4v^2 - (1 + v^2 - u^2)^2}{4uv} \right)^2 \overline{I^2(u, v, k, \eta_R, \eta)} \mathcal{P}_\zeta(uk) \mathcal{P}_\zeta(vk), \quad (\text{D.2})$$

where \mathcal{P}_ζ is the primordial spectrum of the curvature perturbations. Here, $\overline{I^2(u, v, k, \eta_R, \eta)}$ is the time average of I^2 defined by

$$I(u, v, k, \eta_R, \eta) \equiv \int_0^x d\tilde{x} \frac{a(\tilde{\eta})}{a(\eta)} k G_k(\eta, \tilde{\eta}) f(u, v, \tilde{x}, x_{\text{decay}}), \quad (\text{D.3})$$

where $x \equiv k\eta$. Here, $G_k(\eta, \tilde{\eta})$ is Green's function satisfying

$$G_k''(\eta, \tilde{\eta}) + \left(k^2 - \frac{a''(\eta)}{a(\eta)} \right) G_k(\eta, \tilde{\eta}) = \delta(\eta - \tilde{\eta}), \quad (\text{D.4})$$

and f is defined by

$$f(u, v, \tilde{x}, x_{\text{decay}}) \equiv \frac{3 \left[2(5 + 3w(\tilde{\eta}))\mathcal{T}(u\tilde{x})\mathcal{T}(v\tilde{x}) + 4\mathcal{H}^{-1}(\mathcal{T}(u\tilde{x})\mathcal{T}'(v\tilde{x}) + \mathcal{T}'(u\tilde{x})\mathcal{T}(v\tilde{x})) + 4\mathcal{H}^{-2}\mathcal{T}'(u\tilde{x})\mathcal{T}'(v\tilde{x}) \right]}{25(1 + w(\tilde{\eta}))}, \quad (\text{D.5})$$

where $w(\tilde{\eta})$ is the equation-of-state parameter defined by $p = w\rho$ at $\eta = \tilde{\eta}$, and $\mathcal{H} \equiv aH$ is the conformal Hubble parameter. Here, $\mathcal{T}(k\eta)$ is the transfer function of scalar perturbation Φ , defined by $\Phi_{\mathbf{k}} \equiv \phi_{\mathbf{k}}\mathcal{T}(k\eta)$, where $\Phi_{\mathbf{k}}$ is the Fourier component of Φ , and $\phi_{\mathbf{k}}$ is the primordial value of $\Phi_{\mathbf{k}}$.

To calculate $\overline{\mathcal{P}_h(\eta, k)}$, we consider the time evolution of $\mathcal{T}(x)$ by dividing the evolution into four eras: (i) eRD era, (ii) eMD era, (iii) transition period to RD era during L-ball decay process, and (iv) RD era. Firstly, as for era (i), $\Phi(x)$ for superhorizon modes remains almost constant while $\Phi(x)$ for subhorizon modes is suppressed. The transfer function at $\eta = \eta_{\text{eq},1}$ is evaluated by a fitting formula [65, 66]

$$\mathcal{T}(x_{\text{eq},1}) = \frac{\ln[1 + 0.146x_{\text{eq},1}]}{0.146x_{\text{eq},1}} \left[1 + 0.242x_{\text{eq},1} + (1.01x_{\text{eq},1})^2 + (0.341x_{\text{eq},1})^3 + (0.418x_{\text{eq},1})^4 \right]^{-1/4}. \quad (\text{D.6})$$

Secondly, as for era (ii), \mathcal{T} remain constant in the linear theory regime, and density perturbations δ_m grow as $\propto a$. Then, δ_m with a certain mode enters the non-linear regime during the eMD era, and we need to take into account non-linear effects. We assume that the density perturbation in the non-linear regime $\delta_m(k_{\text{NL}})$ and gravitational potential is connected by Poisson equation given by

$$\frac{3}{5}k_{\text{NL}}^2\mathcal{T}(x_{\text{NL}})\mathcal{P}_\zeta^{1/2} = \frac{3}{2}\mathcal{H}^2\delta_{\text{m,NL}}(k_{\text{NL}}), \quad (\text{D.7})$$

where k_{NL} is wave number in non-linear regime and $x_{\text{NL}} \equiv k_{\text{NL}}\eta$. To evaluate the $\delta_{\text{m,NL}}(k_{\text{NL}})$, we adopt the result of N-body simulation in Refs. [67, 68]. According to Refs. [67, 68], $\delta_{\text{m,NL}}(k_{\text{NL}})$ can be related to the value of $\delta_{\text{m,L}}(k_{\text{L}})$, which is the linearly extrapolated density perturbation, by

$$\delta_{\text{m,NL}}^2(k_{\text{NL}}) = f_{\text{NL}}[\delta_{\text{m,L}}^2(k_{\text{L}})], \quad (\text{D.8})$$

where function $f_{\text{NL}}(x)$ has fitting formula given by

$$f_{\text{NL}}(x) = x \left[\frac{1 + 0.4x + 0.498x^4}{1 + 0.00365x^3} \right]^{1/2}, \quad (\text{D.9})$$

and the relation between k_{NL} and k_{L} is given by

$$k_{\text{L}} = [1 + \delta_{\text{m,NL}}^2(k_{\text{NL}})]^{-1/3} k_{\text{NL}}. \quad (\text{D.10})$$

By substituting Poisson equation of δ_{L} to Eq. (D.8), we obtain

$$\delta_{\text{m,NL}}^2(k_{\text{NL}}) = f_{\text{NL}} \left[\frac{4}{25}C^2 A_s \mathcal{H}^{-4} k_{\text{L}}^4 \mathcal{T}(x_{\text{eq},1})^2 \right]. \quad (\text{D.11})$$

By substituting Eqs. (D.9) and (D.11) to Eq. (D.10), we obtain the relation between k_{NL} and k_{L} , denoting as $k_{\text{NL}} = F_{\text{NL}}(k_{\text{L}})$. By substituting $k_{\text{L}} = F_{\text{NL}}^{-1}(k_{\text{NL}})$, Eqs. (D.6) and (D.11) into Eq. (D.7), we obtain $\mathcal{T}(x_{\text{NL}})$. From now on, we write the solution $\mathcal{T}(x_{\text{NL,dec}})$ by $\mathcal{T}(x_{\text{NL,eMD}}) = S_{\text{NL}}\mathcal{T}(x_{\text{eq},1})$, where $x_{\text{NL,eMD}}$ is the value of x right before the L-ball decay. From now on, we omit the subscript ‘‘NL’’.

Thirdly, as for era (iii), \mathcal{T} decays proportionally to the matter density perturbations at first and the time evolution of \mathcal{T} is given by

$$\frac{\mathcal{T}(x)}{\mathcal{T}(x_{\text{eMD}})} \simeq \frac{M_{\text{Q}}(t)}{M_{\text{Q,init}}} \simeq \left(1 - \frac{t}{t_{\text{decay}}} \right)^{3/5}, \quad (\text{D.12})$$

where $M_{\text{Q}}(t)$ is the mass of each L-ball and $M_{\text{Q,init}}$ is the L-ball mass at formation, given by Eq. (3.9). The above equation assumes that gravitational potential is determined by matter density perturbation, which requires

$$3a^2|\ddot{\mathcal{T}}| \ll k^2\mathcal{T}, \quad (\text{D.13})$$

as a necessary condition. We assume that \mathcal{T} begins to be determined by radiation density perturbation once Eq. (D.13) is violated. We denote this period by $\eta = \eta_{\text{dcpl}}$, which satisfies

$$k\eta_{\text{decay}} - k\eta_{\text{dcpl}} = \frac{9\sqrt{2}}{5}. \quad (\text{D.14})$$

Substituting Eq. (D.14) into Eq. (D.12), we obtain the lower bound of \mathcal{T} at the onset of RD, denoted as \mathcal{T}_{low} , given by

$$\mathcal{T}_{\text{low}} \simeq \left(\frac{9\sqrt{2}}{5k\eta_{\text{decay}}} \right)^{3/5} S_{\text{NL}} \mathcal{T}(x_{\text{eq},1}) \equiv S_{\text{decay}} S_{\text{NL}} \mathcal{T}(x_{\text{eq},1}) . \quad (\text{D.15})$$

Note that this \mathcal{T}_{low} gives a lower bound of \mathcal{T} at the onset of RD, because \mathcal{T} can decouple from matter density perturbation even before the necessary condition (D.13) is violated.

Finally, we discuss era (iv). In this period, \mathcal{T} is determined by radiation density perturbations, which oscillate due to pressure on subhorizon scales. Setting $w = 1/3$, the equation of \mathcal{T} is written as

$$\mathcal{T}'' + 4\mathcal{H}\mathcal{T}' + \frac{k^2}{3}\mathcal{T} = 0 . \quad (\text{D.16})$$

The solution with initial condition $\mathcal{T}(x = x_{\text{decay}}) = S_{\text{decay}} S_{\text{NL}} \mathcal{T}(x_{\text{eq},1})$, $\mathcal{T}'(x = x_{\text{decay}}) \simeq 0$ is given by [56, 62]

$$\mathcal{T}(x > x_{\text{decay}}) = S_{\text{decay}} S_{\text{NL}} \mathcal{T}(x_{\text{eq},1}) (A\mathcal{J}(x) + B\mathcal{Y}(x)) . \quad (\text{D.17})$$

Here, $\mathcal{J}(x)$, $\mathcal{Y}(x)$ are defined using first and second spherical Bessel functions, $j_1(x)$ and $y_1(x)$, as

$$\begin{aligned} \mathcal{J}(x) &= \frac{3\sqrt{3}j_1\left(\frac{x-x_{\text{decay}}}{\sqrt{3}}\right)}{x - x_{\text{decay}}/2} , \\ \mathcal{Y}(x) &= \frac{3\sqrt{3}y_1\left(\frac{x-x_{\text{decay}}}{\sqrt{3}}\right)}{x - x_{\text{decay}}/2} , \end{aligned} \quad (\text{D.18})$$

and coefficients A , B are defined by

$$\begin{aligned} A &= \frac{1}{\mathcal{J}(x_{\text{decay}}) - \frac{\mathcal{Y}}{\mathcal{Y}'(x_{\text{decay}})} \mathcal{J}'(x_{\text{decay}})} , \\ B &= -\frac{\mathcal{J}'(x_{\text{decay}})}{\mathcal{Y}'(x_{\text{decay}})} A . \end{aligned} \quad (\text{D.19})$$

By substituting Eqs. (D.3), (D.5), and (D.17) into Eq. (D.2), we finally obtain the gravitational wave spectrum. The approximate analytic result is given by Eq. (4.5).

References

- [1] A. Boyarsky, M. Drewes, T. Lasserre, S. Mertens and O. Ruchayskiy, *Sterile neutrino Dark Matter*, *Prog. Part. Nucl. Phys.* **104** (2019) 1–45, [[1807.07938](#)].
- [2] K. N. Abazajian, *Sterile neutrinos in cosmology*, *Phys. Rept.* **711-712** (2017) 1–28, [[1705.01837](#)].
- [3] S. Dodelson and L. M. Widrow, *Sterile-neutrinos as dark matter*, *Phys. Rev. Lett.* **72** (1994) 17–20, [[hep-ph/9303287](#)].
- [4] K. Abazajian, G. M. Fuller and M. Patel, *Sterile neutrino hot, warm, and cold dark matter*, *Phys. Rev. D* **64** (2001) 023501, [[astro-ph/0101524](#)].

- [5] K. Abazajian, G. M. Fuller and W. H. Tucker, *Direct detection of warm dark matter in the X-ray*, *Astrophys. J.* **562** (2001) 593–604, [[astro-ph/0106002](#)].
- [6] X.-D. Shi and G. M. Fuller, *A New dark matter candidate: Nonthermal sterile neutrinos*, *Phys. Rev. Lett.* **82** (1999) 2832–2835, [[astro-ph/9810076](#)].
- [7] K. Abazajian, *Production and evolution of perturbations of sterile neutrino dark matter*, *Phys. Rev. D* **73** (2006) 063506, [[astro-ph/0511630](#)].
- [8] A. D. Dolgov and S. H. Hansen, *Massive sterile neutrinos as warm dark matter*, *Astropart. Phys.* **16** (2002) 339–344, [[hep-ph/0009083](#)].
- [9] A. Boyarsky, A. Neronov, O. Ruchayskiy and M. Shaposhnikov, *Constraints on sterile neutrino as a dark matter candidate from the diffuse x-ray background*, *Mon. Not. Roy. Astron. Soc.* **370** (2006) 213–218, [[astro-ph/0512509](#)].
- [10] A. Boyarsky, A. Neronov, O. Ruchayskiy, M. Shaposhnikov and I. Tkachev, *Where to find a dark matter sterile neutrino?*, *Phys. Rev. Lett.* **97** (2006) 261302, [[astro-ph/0603660](#)].
- [11] R. Shrock, *Decay $l0 \rightarrow \nu(\text{lepton}) \gamma$ in gauge theories of weak and electromagnetic interactions*, *Phys. Rev. D* **9** (1974) 743–748.
- [12] J. W. den Herder et al., *The Search for decaying Dark Matter*, [0906.1788](#).
- [13] J. Baur, N. Palanque-Delabrouille, C. Yeche, A. Boyarsky, O. Ruchayskiy, E. Armengaud et al., *Constraints from Ly- α forests on non-thermal dark matter including resonantly-produced sterile neutrinos*, *JCAP* **12** (2017) 013, [[1706.03118](#)].
- [14] M. Viel, J. Lesgourgues, M. G. Haehnelt, S. Matarrese and A. Riotto, *Constraining warm dark matter candidates including sterile neutrinos and light gravitinos with WMAP and the Lyman-alpha forest*, *Phys. Rev. D* **71** (2005) 063534, [[astro-ph/0501562](#)].
- [15] G. B. Gelmini, P. Lu and V. Takhistov, *Cosmological Dependence of Resonantly Produced Sterile Neutrinos*, *JCAP* **06** (2020) 008, [[1911.03398](#)].
- [16] A. Boyarsky, O. Ruchayskiy and M. Shaposhnikov, *The Role of sterile neutrinos in cosmology and astrophysics*, *Ann. Rev. Nucl. Part. Sci.* **59** (2009) 191–214, [[0901.0011](#)].
- [17] C. T. Kishimoto and G. M. Fuller, *Lepton Number-Driven Sterile Neutrino Production in the Early Universe*, *Phys. Rev. D* **78** (2008) 023524, [[0802.3377](#)].
- [18] M. Laine and M. Shaposhnikov, *Sterile neutrino dark matter as a consequence of νMSM -induced lepton asymmetry*, *JCAP* **06** (2008) 031, [[0804.4543](#)].
- [19] J. Ghiglieri and M. Laine, *Improved determination of sterile neutrino dark matter spectrum*, *JHEP* **11** (2015) 171, [[1506.06752](#)].
- [20] A. Matsumoto et al., *EMPRESS. VIII. A New Determination of Primordial He Abundance with Extremely Metal-poor Galaxies: A Suggestion of the Lepton Asymmetry and Implications for the Hubble Tension*, *Astrophys. J.* **941** (2022) 167, [[2203.09617](#)].
- [21] M. Kawasaki, F. Takahashi and M. Yamaguchi, *Large lepton asymmetry from Q balls*, *Phys. Rev. D* **66** (2002) 043516, [[hep-ph/0205101](#)].
- [22] M. Kawasaki and K. Murai, *Lepton asymmetric universe*, *JCAP* **08** (2022) 041, [[2203.09713](#)].
- [23] M. Shaposhnikov, *The νMSM , leptonic asymmetries, and properties of singlet fermions*, *JHEP* **08** (2008) 008, [[0804.4542](#)].
- [24] A. Sesana et al., *Unveiling the gravitational universe at μ -Hz frequencies*, *Exper. Astron.* **51** (2021) 1333–1383, [[1908.11391](#)].
- [25] THEIA collaboration, M. Askins et al., *THEIA: an advanced optical neutrino detector*, *Eur. Phys. J. C* **80** (2020) 416, [[1911.03501](#)].

- [26] K. Abazajian, N. F. Bell, G. M. Fuller and Y. Y. Y. Wong, *Cosmological lepton asymmetry, primordial nucleosynthesis, and sterile neutrinos*, *Phys. Rev. D* **72** (2005) 063004, [[astro-ph/0410175](#)].
- [27] A. D. Dolgov, *Neutrinos in cosmology*, *Phys. Rept.* **370** (2002) 333–535, [[hep-ph/0202122](#)].
- [28] D. Notzold and G. Raffelt, *Neutrino Dispersion at Finite Temperature and Density*, *Nucl. Phys. B* **307** (1988) 924–936.
- [29] G. B. Gelmini, P. Lu and V. Takhistov, *Cosmological Dependence of Non-resonantly Produced Sterile Neutrinos*, *JCAP* **12** (2019) 047, [[1909.13328](#)].
- [30] A. D. Dolgov, S. H. Hansen, S. Pastor, S. T. Petcov, G. G. Raffelt and D. V. Semikoz, *Cosmological bounds on neutrino degeneracy improved by flavor oscillations*, *Nucl. Phys. B* **632** (2002) 363–382, [[hep-ph/0201287](#)].
- [31] Y. Y. Y. Wong, *Analytical treatment of neutrino asymmetry equilibration from flavor oscillations in the early universe*, *Phys. Rev. D* **66** (2002) 025015, [[hep-ph/0203180](#)].
- [32] T. Asaka, M. Laine and M. Shaposhnikov, *Lightest sterile neutrino abundance within the nuMSM*, *JHEP* **01** (2007) 091, [[hep-ph/0612182](#)].
- [33] T. Asaka, M. Laine and M. Shaposhnikov, “Imaginary part of the active neutrino self-energy at $T < 10$ GeV.” <http://www.laine.itp.unibe.ch/neutrino-rate/>.
- [34] O. Wantz and E. P. S. Shellard, *Axion Cosmology Revisited*, *Phys. Rev. D* **82** (2010) 123508, [[0910.1066](#)].
- [35] K. Petraki and A. Kusenko, *Dark-matter sterile neutrinos in models with a gauge singlet in the Higgs sector*, *Phys. Rev. D* **77** (2008) 065014, [[0711.4646](#)].
- [36] A. Kusenko, F. Takahashi and T. T. Yanagida, *Dark Matter from Split Seesaw*, *Phys. Lett. B* **693** (2010) 144–148, [[1006.1731](#)].
- [37] I. Affleck and M. Dine, *A New Mechanism for Baryogenesis*, *Nucl. Phys. B* **249** (1985) 361–380.
- [38] M. Dine, L. Randall and S. D. Thomas, *Baryogenesis from flat directions of the supersymmetric standard model*, *Nucl. Phys. B* **458** (1996) 291–326, [[hep-ph/9507453](#)].
- [39] H. Murayama and T. Yanagida, *Leptogenesis in supersymmetric standard model with right-handed neutrino*, *Phys. Lett. B* **322** (1994) 349–354, [[hep-ph/9310297](#)].
- [40] T. Gherghetta, C. F. Kolda and S. P. Martin, *Flat directions in the scalar potential of the supersymmetric standard model*, *Nucl. Phys. B* **468** (1996) 37–58, [[hep-ph/9510370](#)].
- [41] A. de Gouvea, T. Moroi and H. Murayama, *Cosmology of supersymmetric models with low-energy gauge mediation*, *Phys. Rev. D* **56** (1997) 1281–1299, [[hep-ph/9701244](#)].
- [42] A. Kusenko and M. E. Shaposhnikov, *Supersymmetric Q balls as dark matter*, *Phys. Lett. B* **418** (1998) 46–54, [[hep-ph/9709492](#)].
- [43] K. Enqvist and J. McDonald, *Q balls and baryogenesis in the MSSM*, *Phys. Lett. B* **425** (1998) 309–321, [[hep-ph/9711514](#)].
- [44] S. Kasuya and M. Kawasaki, *Q ball formation through Affleck-Dine mechanism*, *Phys. Rev. D* **61** (2000) 041301, [[hep-ph/9909509](#)].
- [45] S. Kasuya and M. Kawasaki, *Baryogenesis from the gauge-mediation type Q-ball and the new type of Q-ball as the dark matter*, *Phys. Rev. D* **89** (2014) 103534, [[1402.4546](#)].
- [46] S. Kasuya and M. Kawasaki, *Q ball formation: Obstacle to Affleck-Dine baryogenesis in the gauge mediated SUSY breaking?*, *Phys. Rev. D* **64** (2001) 123515, [[hep-ph/0106119](#)].
- [47] S. Kasuya, M. Kawasaki and M. Yamada, *Revisiting the gravitino dark matter and baryon asymmetry from Q-ball decay in gauge mediation*, *Phys. Lett. B* **726** (2013) 1–7, [[1211.4743](#)].

- [48] J. Hisano, M. M. Nojiri and N. Okada, *The Fate of the B ball*, *Phys. Rev. D* **64** (2001) 023511, [[hep-ph/0102045](#)].
- [49] A. G. Cohen, S. R. Coleman, H. Georgi and A. Manohar, *The Evaporation of Q Balls*, *Nucl. Phys. B* **272** (1986) 301–321.
- [50] M. Kawasaki and M. Yamada, *Q ball Decay Rates into Gravitinos and Quarks*, *Phys. Rev. D* **87** (2013) 023517, [[1209.5781](#)].
- [51] M. Laine and M. E. Shaposhnikov, *Thermodynamics of nontopological solitons*, *Nucl. Phys. B* **532** (1998) 376–404, [[hep-ph/9804237](#)].
- [52] R. Banerjee and K. Jedamzik, *On B-ball dark matter and baryogenesis*, *Phys. Lett. B* **484** (2000) 278–282, [[hep-ph/0005031](#)].
- [53] M. Kawasaki, K. Kohri, T. Moroi and Y. Takaesu, *Revisiting Big-Bang Nucleosynthesis Constraints on Long-Lived Decaying Particles*, *Phys. Rev. D* **97** (2018) 023502, [[1709.01211](#)].
- [54] J. Baur, N. Palanque-Desabrouille, C. Yèche, C. Magneville and M. Viel, *Lyman-alpha Forests cool Warm Dark Matter*, *JCAP* **08** (2016) 012, [[1512.01981](#)].
- [55] A. Neronov, D. Malyshev and D. Eckert, *Decaying dark matter search with NuSTAR deep sky observations*, *Phys. Rev. D* **94** (2016) 123504, [[1607.07328](#)].
- [56] K. Inomata, K. Kohri, T. Nakama and T. Terada, *Enhancement of gravitational waves induced by scalar perturbations due to a sudden transition from an early matter era to the radiation era*, *J. Phys. Conf. Ser.* **1468** (2020) 012002.
- [57] S. Kasuya, M. Kawasaki and K. Murai, *Enhancement of second-order gravitational waves at Q-ball decay*, *JCAP* **05** (2023) 053, [[2212.13370](#)].
- [58] M. Kawasaki and K. Murai, *Enhancement of gravitational waves at Q-ball decay including non-linear density perturbations*, [2308.13134](#).
- [59] G. White, L. Pearce, D. Vagie and A. Kusenko, *Detectable Gravitational Wave Signals from Affleck-Dine Baryogenesis*, *Phys. Rev. Lett.* **127** (2021) 181601, [[2105.11655](#)].
- [60] M. Pearce, L. Pearce, G. White and C. Balázs, *Gravitational Wave Signals From Early Matter Domination: Interpolating Between Fast and Slow Transitions*, [2311.12340](#).
- [61] PLANCK collaboration, N. Aghanim et al., *Planck 2018 results. VI. Cosmological parameters*, *Astron. Astrophys.* **641** (2020) A6, [[1807.06209](#)].
- [62] K. Kohri and T. Terada, *Semianalytic calculation of gravitational wave spectrum nonlinearly induced from primordial curvature perturbations*, *Phys. Rev. D* **97** (2018) 123532, [[1804.08577](#)].
- [63] K. N. Ananda, C. Clarkson and D. Wands, *The Cosmological gravitational wave background from primordial density perturbations*, *Phys. Rev. D* **75** (2007) 123518, [[gr-qc/0612013](#)].
- [64] D. Baumann, P. J. Steinhardt, K. Takahashi and K. Ichiki, *Gravitational Wave Spectrum Induced by Primordial Scalar Perturbations*, *Phys. Rev. D* **76** (2007) 084019, [[hep-th/0703290](#)].
- [65] J. M. Bardeen, J. R. Bond, N. Kaiser and A. S. Szalay, *The Statistics of Peaks of Gaussian Random Fields*, *Astrophys. J.* **304** (1986) 15–61.
- [66] K. Inomata, M. Kawasaki, K. Mukaida, T. Terada and T. T. Yanagida, *Gravitational Wave Production right after a Primordial Black Hole Evaporation*, *Phys. Rev. D* **101** (2020) 123533, [[2003.10455](#)].
- [67] A. J. S. Hamilton, A. Matthews, P. Kumar and E. Lu, *Reconstructing the primordial spectrum of fluctuations of the universe from the observed nonlinear clustering of galaxies*, *Astrophys. J. Lett.* **374** (1991) L1.
- [68] J. A. Peacock and S. J. Dodds, *Reconstructing the linear power spectrum of cosmological mass fluctuations*, *Mon. Not. Roy. Astron. Soc.* **267** (1994) 1020–1034, [[astro-ph/9311057](#)].